

HEAT PIPE RESEARCH AND DEVELOPMENT IN THE AMERICAS

FLAVIO DOBRAN

New York University, Applied Science Department, New York, NY 10003, U.S.A.

Abstract—The purpose of this paper is to present a review of the recent heat pipe research and development efforts in the Americas. After discussing the research and development of high performance monogroove, tapered artery, trapezoidally grooved, dual-slot, double wall artery, ceramic and other specially designed heat pipes, the transient modeling and testing efforts are reviewed for a variety of heat pipes that also includes variable conductance heat pipes and thermosyphons. The application of heat pipes to terrestrial systems is discussed for the heat recovery systems, Rankine and solar systems, fusion reactor core cooling and the thermal control of electronic equipment. The application of heat pipes to space systems includes the thermal control of space station and satellites, and the radiator design of large space power systems. Although many advances have been made in the past few years in the development of high heat transfer performance heat pipes, the heat pipe modeling efforts are not in step with the technological requirements.

NOMENCLATURE

A	area
B	magnetic field
C_p	specific heat at constant pressure
Ca	capillary number, $\mu_l^2/(\sigma\rho_l D)$
D	tube diameter
g	gravitational constant
h^*	liquid filling height in a thermosyphon, $V_L/(\pi R^3)$
h_h	enthalpy of evaporation
\bar{h}	heat transfer coefficient
h_s	static wicking height
k_{eff}	effective thermal conductivity
l	liquid filling height in a thermosyphon
l^*	L/R
L	pipe length
L_{eff}	effective length for heat transport, $0.5(L_c + L_e) + L_a$
L_f^*	l/L_e
m	mass
N_L	two-phase Grashof number, $(gD^3\rho_l^2/\mu_l^2)^{0.5}$
P	pressure
Q	heat flux
Q_f^*	$Q_l/(8\mu_l R h_h)$
R	tube radius
S	composite factor
t	time
T	temperature
V_L	liquid filling
w	width
α	groove aspect ratio (groove depth/width)
Γ	mass flow rate per unit tube periphery
δ	depth of surface texturing or channel thickness
$\bar{\delta}$	average film thickness
μ	viscosity
μ^*	μ_c/μ_l
ρ	density
ρ^*	ρ_c/ρ_l
σ	surface tension
Σ	electrical conductivity
<i>Subscripts</i>	
a	pertains to the adiabatic region of heat pipe
amb	ambient condition of heat pipe
c	pertains to the condenser region of heat pipe

<i>e</i>	pertains to the evaporator region of heat pipe
<i>eff</i>	effective
<i>i</i>	inside or input
<i>l, L</i>	pertains to the liquid
<i>o</i>	outside
<i>r</i>	radial
<i>t</i>	total
<i>v, V</i>	pertains to the vapor
<i>w</i>	pertains to the wall

1. INTRODUCTION

A significant portion of the heat pipe research and development efforts in the Americas, and primarily in the United States, pertains to space applications. The United States is designing a space station, space platforms and a large space power generating system, which will primarily use heat pipes in radiators to dissipate large amounts of thermal energy into Space. The thermal control of satellites continues to use heat pipes very effectively over a wide temperature range. The terrestrial heat pipe application fields involve heat recovery systems, thermal control of electronic equipment, solar heating, etc. The specific application determines the heat pipe's global design characteristics (operating temperature, working fluid and material of its construction), whereas the nature of the application determines the heat pipe's detailed design characteristics (the internal liquid and vapor flow geometry and external shape as well as the evaporator and condenser orientation with respect to the gravity field vector). The heat pipe application temperatures may range from a liquid helium temperature of a few degrees Kelvin to a thousand or more degrees as in the cooling of combustion chambers and envisioned space nuclear reactor cores. The detailed nature of the application dictates whether a heat pipe is used for separating the heat source from the heat sink, temperature control, heat flux transformation, etc.

Heat pipes may be classified broadly into thermosyphons and all other heat pipes. Among these, the thermosyphons are the simplest and utilize gravity for the condensate return from the condenser to the evaporator. The remaining heat pipes may use wicks in the form of screens, fibers or sintered powders, where the condensate return is possible by the capillary forces. Centrifugal, electrostatic, electromagnetic and osmotic forces may also be utilized for the condensate flow return. The gravity force in these heat pipes may aid or hinder the liquid and vapor flow.

Although the basic principle of heat pipe operation is qualitatively well understood, the thermohydrodynamic flow aspects are complicated and determine, for a given geometry pipe and working fluid, its heat transfer limits. High heat fluxes in the evaporator may lead to the burnout condition as a result of the liquid depletion on the surface of the evaporator. The result of such a reduced cooling effectiveness leads to large localized surface temperatures that may produce the destruction of the heat pipe wall. With a small amount of liquid in the evaporator, a dry-out condition may be reached with consequences similar to the burn-out condition. The capillary wick of a heat pipe will function properly if the liquid wets the surface of the porous wick structure, because the liquid will then be readily drawn into and saturate the wick pores by the surface tension force. If the applied heat flux is above the capillary limit flux, an effective liquid supply (pumping) from the condenser to the evaporator will cease. The difference in the shape of the effective surface interface between the evaporator and condenser creates an effective pressure gradient, which causes the liquid to flow through the wick structure from the condenser to the evaporator. This pressure gradient increases with small wick pores, but at the expense of the simultaneous increase in the liquid flow resistance. At high axial heat fluxes and in long heat pipes, the countercurrent flow of liquid and vapor may produce an interfacial instability that results in the liquid droplet entrainment from the liquid into the vapor, or an entrainment limiting operation where any further increase in the vapor flow (as by the heat addition) can no longer sustain an increase in the liquid condensate flow. Another limiting operation is caused by the sonic or choked flow condition, where the vapor flow rate cannot be increased anymore at the expense of larger evaporator heat fluxes and a given condenser temperature. Near the working fluid's freezing point its vapor density, vapor pressure and mass flow rate are low, whereas close to its thermodynamic critical point its properties vary significantly, yielding an erratic heat pipe behavior with the small changes of heat flux or temperature boundary conditions. High density fluids, such as water,

methanol, mercury and cesium, are sensitive to the gravitational effects, whereas the low density fluids, such as sodium and lithium, are much less sensitive and may not severely impede the heat pipe operation in an adverse gravitational field.

Heat pipes must pass through transient states before reaching the steady state operation. The heat pipe starting dynamics depend on the initial working fluid condition, internal and external heat pipe geometry and on the methods of heating and cooling. Excessively large heat transfer rates can cause local wick dry-outs. With a high initial vapor density a very rapid starting occurs (seconds), whereas when this density is low or fluid is frozen, the heat pipe transient can be very long (hours) and may result in a frontal start-up as opposed to a uniform start-up. A heat pipe start-up from the supercritical state can be slow because at first this requires the vapor cooling and condensation. Finally, with the presence of a non-condensable gas in the heat pipe (either intentionally added for an accurate temperature control or unintentionally being present), at first the transient will involve the displacement of the gas into the condenser region prior to the establishment of the normal operation.

This brief review of complex thermohydrodynamic processes in heat pipes not only serves the purpose of illustrating the complexity of an optimal heat pipe design, but also points out that the heat pipe designer has many parameters at his disposal to achieve an optimal design for many applications. The presentation of the recent heat pipe research and development efforts in the Americas will involve, at first, a review of the design and development of the high performance heat pipes. This will then be followed with a review of transient heat pipe modeling and testing efforts, and concluded with a review of heat pipe applications to terrestrial and space systems.

2. HEAT PIPE RESEARCH AND DEVELOPMENT EFFORTS

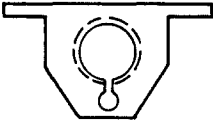

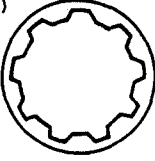
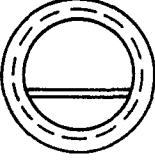
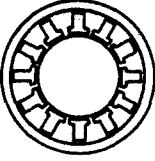
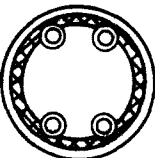
A given application characterizes the heat pipe's operating temperature, best working fluid and material of its construction. For a given working fluid, the maximum heat transfer capacity of a heat pipe will depend on its geometric design characteristics and on how the heat is supplied in the evaporator and withdrawn in the condenser. By judiciously choosing these characteristics, it may be possible to eliminate one or more heat pipe operating limits as discussed above. All current high heat transfer performance heat pipes were designed with such a judicious choice of geometry for the most effective liquid-vapor circulation to maximize the heat transport capacity and structural integrity. Table 1 illustrates the wick geometry and transport capabilities of the recent advanced heat pipe concepts to be discussed first.

2.1. *Specific heat pipe developments*

2.1.1. *Monogroove heat pipe.* The monogroove heat pipe shown in Fig. 1 contains two axial channels: one for the vapor flow and the other for the liquid flow [1]. The slot separating the two channels serves the purpose of creating a high capillary pressure difference. The vapor channel contains circumferential grooves for distributing the liquid flowing through the slot. The two channel design provides a considerable separation between the liquid and vapor flows, and for the most part, eliminates the countercurrent flow limiting operation. Moreover, the liquid viscous pressure drop is minimal because the liquid flows through a channel without obstructions, as opposed to the conventional wick type heat pipe designs. The circumferential grooves in the vapor channel not only provide an effective liquid distribution, but also maximize the heat transfer area for the evaporation of liquid. The heat transfer to and from the heat pipe occurs through the radiator fin attached to the vapor channel as shown in Fig. 1.

Figure 2 shows the pressure balance relations for the monogroove heat pipe. The first equation represents the balance of circumferential or wall wick capillary pressure rise against the viscous pressure drop in the liquid channel, vapor channel and wall grooves, and against the gravities of heat pipe tilt and liquid pumping in the wall grooves. The second relation in Fig. 2 shows a requirement for the monogroove slot to develop a capillary pressure rise to overcome the viscous losses of liquid and vapor in the channels and adverse heat pipe tilt. By expressing each of the pressure drop and rise terms in terms of fluid properties and heat pipe geometry by the well established relations, it is possible to generate the results shown in Fig. 3 [1]. This figure shows the monogroove's heat transport capacity (axial heat flux multiplied by the effective transport

Table 1. Current high performance heat pipe concepts

Wick design	Performance specification
Monogroove (Al extrusion) 	NH ₃ tests: at 21°C $L_{eff} = 4.6\text{ m}$ $D_v = 13.4\text{ mm}$, $D_i = 6.32\text{ mm}$ Slot gap width = 0.254 mm $Q_i L_{eff} = 3,330\text{ W-m}$ (max. no tilt) $Q_r = 13.4\text{ W cm}^{-2}$ Developer: Grumman
Tapered artery (Al extrusion) 	NH ₃ tests: see Table 2 also $L_{eff} = 5.45\text{ m}$ $D_v = 12.2\text{ mm}$, $D_i = 6.35\text{ mm}$ Slot gap width = 0.254 mm $Q_i L_{eff} = 5,200\text{ W-m}$ (max. no tilt) $Q_r = 15\text{ W cm}^{-2}$ Developer: Lockheed
Trapezoidal axially grooved (Al) 	NH ₃ tests: 20–70°C $L_{eff} = 2.97\text{ m}$, $D_o = 41\text{ mm}$, 32 grooves Groove width: 0.13–0.8 mm Groove depth: 4.0–4.4 mm $Q_i L_{eff} = 11,000\text{ W-m}$ (3 mm adv. tilt) $Q_r = 2.8\text{ W cm}^{-2}$ Developer: OAO Corporation
Dual slot 	Methanol analysis: 120°C $L_{eff} = 4\text{ m}$, $D_o = 25.4\text{ mm}$ $Q_i L_{eff} = 18,600\text{ W-m}$ (max. no tilt) Stainless steel Developer: Grumman
Double wall artery (copper) 	Water tests: 100°C $L_{eff} = 1.72\text{ m}$, $D_o = 22.2\text{ mm}$, $D_v = 12.7\text{ mm}$ $Q_i L_{eff} = 2,100\text{ W-m}$ (max. no tilt and 166°C) $Q_r = 16\text{ W cm}^{-2}$ Developer: Wright Aeronautical Laboratories
Dual pair artery liquid metal (Molybdenum alloy) 	Lithium tests: 1230°C $L_{eff} = 1.6\text{ m}$ $D_o = 15.8\text{ mm}$, $D_i = 14.2\text{ mm}$ 1.5 mm artery diameter 400 mesh screen $Q_i L_{eff} = 48,000\text{ W-m}$ $Q_r = 150\text{ W cm}^{-2}$ Developer: Los Alamos National Laboratory

length) with ammonia as the working fluid, as a function of the liquid channel diameter, slot gap width and adverse tilt. The curves labeled "monogroove limited" correspond to an operating limit caused by the capillary pressure rise across the slot, whereas the curves labeled "wall wick limited" correspond to the limiting capillary pressure rise in the circumferential grooves. The analytical results in Fig. 3a show that small liquid channel diameters produce a limiting operation as a result of an excessive viscous pressure drop in the channel, whereas large liquid channel diameters yield a limiting performance due to the wall wick capillary pressure rise. These results clearly imply the existence of an optimum liquid channel diameter and that with such a selected diameter the heat

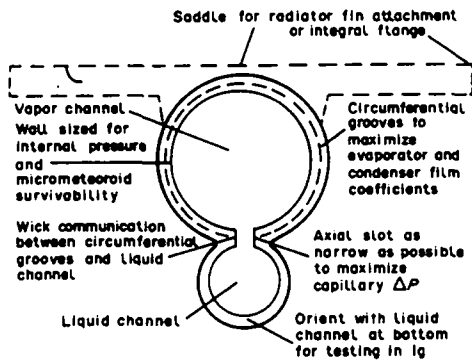


Fig. 1. Monogroove heat pipe configuration.
Copyright ©AIAA; reprinted with permission.

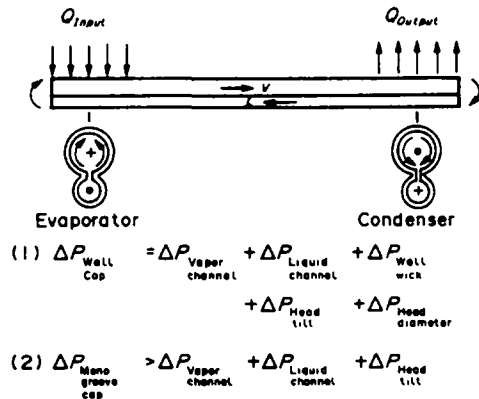


Fig. 2. Monogroove heat pipe operating principles.
Copyright ©AIAA; reprinted with permission.

transport capacity is relatively insensitive to the slot gap width as illustrated in Fig. 3b. Figure 3c shows the sensitivity of heat pipe's transport capacity to adverse tilts, where one may note that the performance can deteriorate rapidly with large tilts. The separation of liquid and vapor channels and the addition of heat through the fin attached to the vapor channel resist the heat pipe's boiling limited operation and provide for the venting of bubbles through the slot when they happen to be entrained in the liquid channel. When the bubbles become entrained in the liquid channel, however, a reduction of the heat pipe load is necessary to reprime it and start the heat pipe operation. Figure 4 illustrates a comparison between the predicted heat pipe performance and tests conducted with a 5.5 m test article, showing that the performance is wall wick limited at low tilts and monogroove limited at higher tilts. The predicted steady state performance is generally overestimated up to 15 per cent.

2.1.2. Tapered artery heat pipe. As noted in the preceding description of the monogroove heat pipe, the presence of a noncondensable gas or vapor in the liquid channel can lead to the heat pipe depriming and loss of performance. The tapered artery heat pipe, shown in Fig. 5, is similar in design and operation to the monogroove heat pipe, but with provision for automatic bubble or gas venting from the liquid channel by means of a tapered liquid arterial channel [2]. Figure 6 illustrates the automatic bubble venting process.

During normal operation, only liquid flows through the liquid arterial channel (Fig. 6A). As a bubble is created in the channel as a result of the boiling of the liquid or the presence of a noncondensable gas, for example, the circumferential grooves begin to dry because of the lack of liquid supply and the slot meniscus begins to recede into the base of the grooves (Fig. 6B). Further heat addition produces the superheat of liquid in the artery (Fig. 6C) and minisci coalescence (Fig. 6D) with the consequence that the bubble in the liquid channel then vents into the vapor channel. The tapered shape of the liquid arterial channels also provides meniscus stability and prevents the flow choking owing to an increased flow rate of liquid from the channel to the wall grooves as the heat flux increases. This prevents, then, the boiling in the channel.

Table 2 summarizes different tapered artery heat pipe tests, whereas Fig. 7 illustrates the results with a 6.7 m long test article and cross sectional geometry as given in Fig. 5. The significant results from these tests are as follows: (1) the working fluid overcharge has a negligible effect on performance, whereas an undercharge reduces performance; (2) the heat pipe requires no priming foils or screens; (3) the heat pipe length affects the start-up capability, requiring little power input for long pipes to provide sufficient circulation of the working fluid several times through the system; (4) a rapid condenser cool down may produce liquid superheating and flash boiling (the tests show that the heat pipe can recover from such situations); (5) the freeze/thaw tests demonstrate the depriming and repriming (bubble venting) capability of the heat pipe; and (6) the radial flux densities achieved rose to 15 W cm^{-2} with ammonia as the working fluid.

2.1.3. Advanced trapezoidal axially grooved (ATAG) heat pipe. Richter and Brennan [3] describe the development of ATAG heat pipes with the objective of providing constructible radiators for

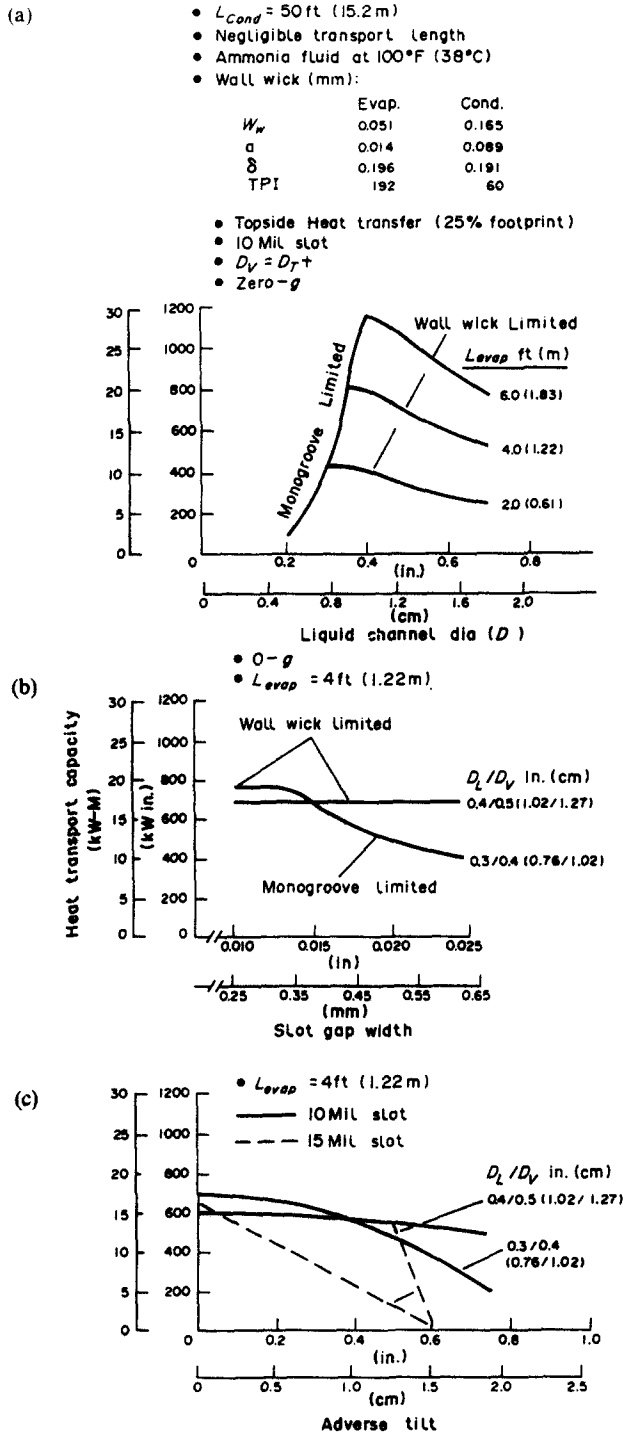


Fig. 3. Monogroove heat pipe heat transport capacity vs: (a) liquid channel diameter; (b) slot gap width; (c) adverse tilt.
Copyright ©AIAA; reprinted with permission.

heat dissipation from space (see below) with the 1 g heat transport capacity goal greater than 30 kW-m at 20°C. In contrast to the previously discussed heat pipes, the ATAG heat pipes have the following characteristics: (1) a round cross-section; (2) 1 g performance can be demonstrated without the gravity assist during priming; (3) axially-grooved heat pipes are not very susceptible to depriming as a result of subcooling and boiling.

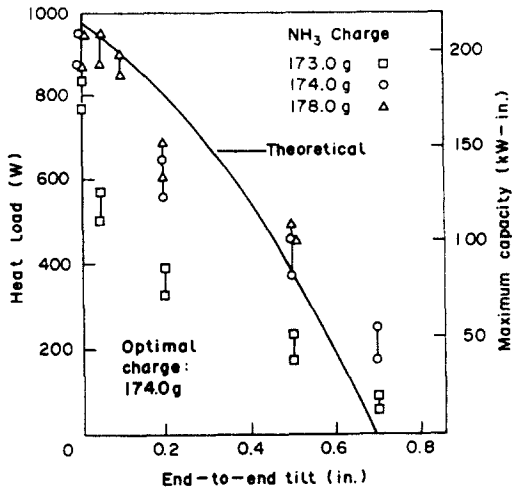


Fig. 7. Results from 6.7 m long tapered artery heat pipe tests.
Copyright ©AIAA; reprinted with permission.

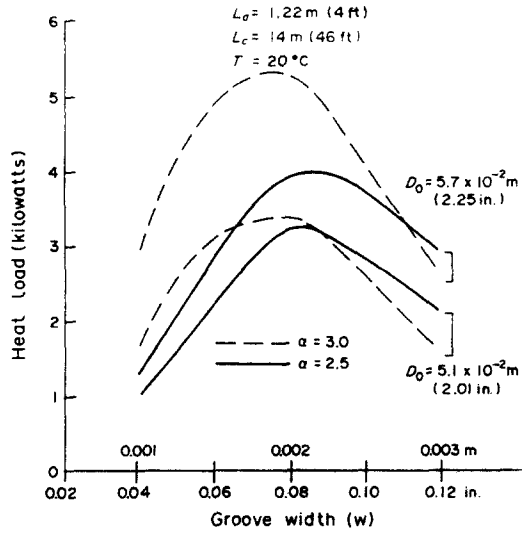


Fig. 8. ATAG's heat transport capacity variation with the groove width.
Copyright ©AIAA; reprinted with permission.

Table 2. Tapered artery heat pipe test configurations
Copyright ©AIAA; reprinted with permission

Configuration	Purpose	Test results
6.7 m heat pipe	Capacity correlation Tolerance to NCG Boiling tolerance Sensitivity to charge	Agreed with theory Requires slow start-up No boiling in artery Sensitive to undercharge
Flexible 2.4 m heat pipe	Capacity	Flex. section degrades capacity
0 g simulation	Internal design for bubble venting	Start-up and freeze/thaw partially demonstrated
3 m heat pipe	Rapid cool down tests	Leads to momentary artery boiling with recovery
10 m heat pipe	Start-up Freeze-thaw tolerance with NCG present	Always possible Depriming and repriming demonstrated

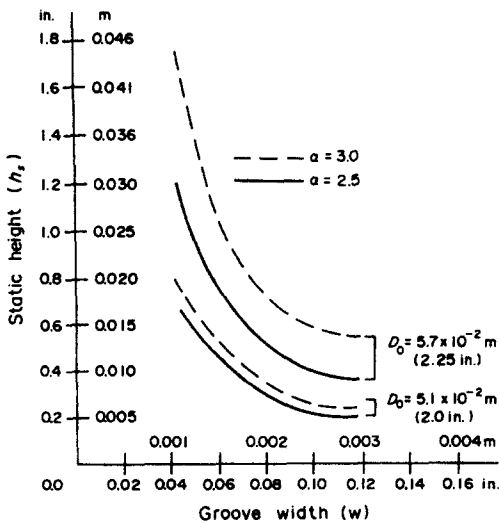


Fig. 9. ATAG's static height variation with the groove width.
Copyright ©AIAA; reprinted with permission.

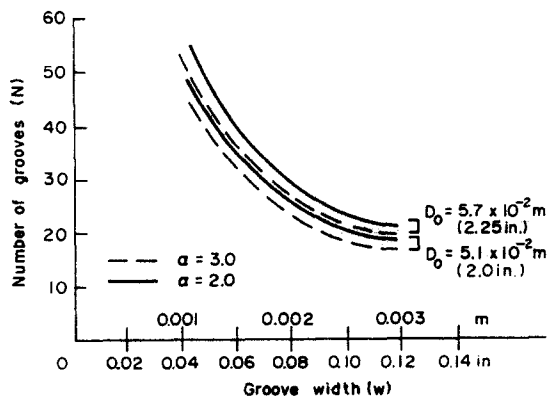


Fig. 10. Number of grooves vs the groove width.
Copyright ©AIAA; reprinted with permission.

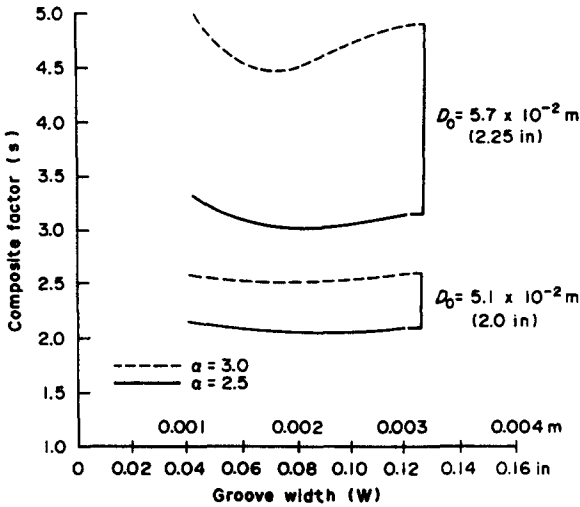


Fig. 11. ATAG's composite factor variation with the groove width.
Copyright ©AIAA; reprinted with permission.

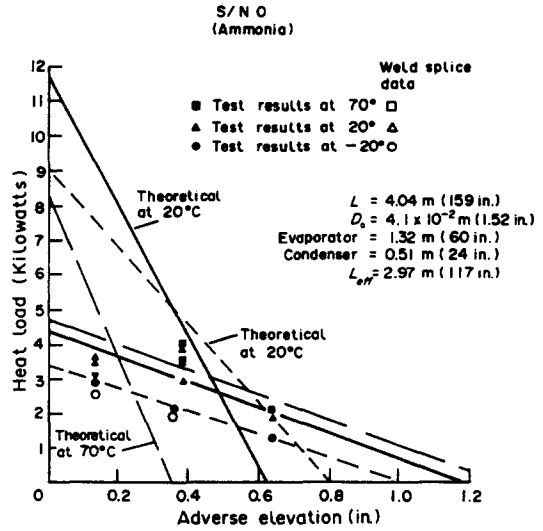


Fig. 12. ATAG's tests compared with predictions.
Copyright ©AIAA; reprinted with permission.

height. For heat pipe loads below 10 KW, the calculations also showed that the entrainment and sonic limits do not present problems. Figure 12 shows some of the test results conducted on a 4.27 m long ATAG heat pipe with ammonia, together with the predicted performance at two different operating temperatures. The deviation between the predicted performance and test data in this figure may be attributed to the heat flux limited performance due to boiling. The achieved performance of 11 kW-m and radial heat flux of 2.8 W cm^{-2} at 20°C with an evaporator length of 1.22 m is below the required performance of 30 kW-m that can be attained with an evaporator length of 1.96 m. The 15.2 m long prototype ATAG heat pipe is presently being fabricated from 4.5 m long sections of ATAG tubing extruded from an aluminum alloy.

2.1.4. *Dual slot heat pipe.* Table 1 shows the dual slot heat pipe cross-sectional geometry and Fig. 13 shows it as integrated into a radiator panel. This heat pipe, patented by Grumman [4], consists of a flat baffle that separates the vapor channel from the liquid channel. The circumferential grooves, machined on the inside of the circular tube, provide the capillary wicking action to transport the working fluid in the evaporator from the liquid channel to the vapor channel, by means of the surface tension. In the condenser section the circumferential grooves provide a path for the condensate to flow from the vapor to the liquid channel. The meniscus between the two slots formed where the baffle touches the inner wall of the tube sustains the pumping pressure differential. Figure 14 [5] shows the predicted performance of this heat pipe for the working fluid methanol and different pipe diameters. At small pipe diameters, the thermal transport capacity is low owing to the small cross-sectional area for fluid flow, whereas at large diameters it is low again

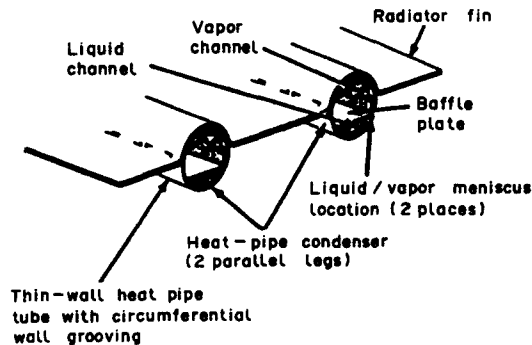


Fig. 13. Schematic of the dual-slot heat pipe and its radiator panel integration.
Copyright ©AIAA; reprinted with permission.

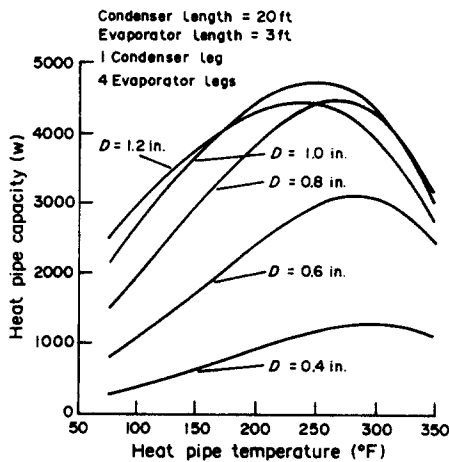


Fig. 14. Predicted dual-slot performance using methanol. Copyright ©AIAA; reprinted with permission.

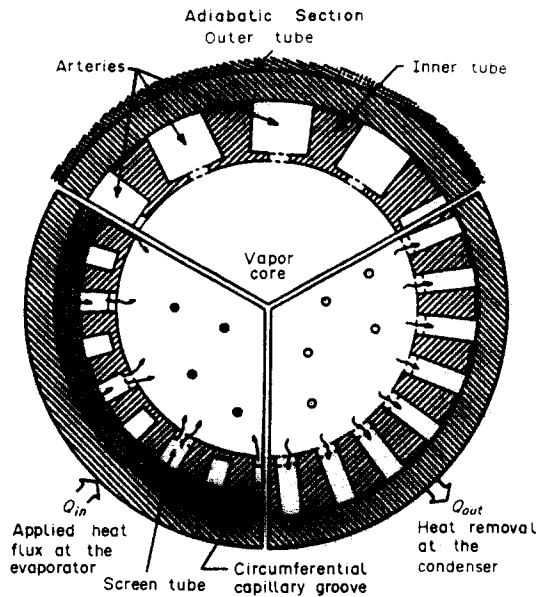


Fig. 15. Double wall artery heat pipe configuration. Copyright ©AIAA; reprinted with permission.

because of the increased resistance to fluid flow in the circumferential grooves. The maximum predicted heat transport capacity of the heat pipe is more than 18 kW-m for the heat pipe length dimensions given in Fig. 14.

2.1.5. *Double wall artery heat pipe (DWA)*. The high performance DWA heat pipe has been under the development for several years at the Wright Aeronautical Laboratories [6-8] (Fig. 15). The improved and latest design, shown in this figure, consists of a composite wick geometry, where the liquid and vapor flow paths have been separated and high radial heat transfer rates achieved through the careful design of the liquid arteries close to the pipe wall. The heat pipe consists of a concentric tube arrangement with the inner tube externally grooved for the liquid transport and slotted to allow for the vapor venting. The evaporator section also includes a screen between the inner surface of the outer pipe and outer grooved surface of the inner slotted pipe for the purpose of maximizing heat transfer and self-priming capability. The latest design eliminates the screens in the adiabatic and condenser regions, which produced higher flow and heat transfer resistances when used in previous designs of this heat pipe.

Table 3 shows a summary of the DWA heat pipe design details. The experimental tests involved the steady state operation to ascertain the predicted transport capacity of 6.5 kW-m. The achieved heat transport capacity was, however, only 2.1 kW-m at 166°C with 1.225 KW input power and 1.72 m effective length, and reduced to 1.5 kW-m at an adverse tilt of 0.3° (with the evaporator end 1 cm higher than the condenser end). The performance results at zero and adverse tilts are shown in Figs 16 and 17, respectively.

Table 3. Double wall artery heat pipe design details

Material: Body and wick: copper			
Working fluid: 130 cm ³ of water			
Overall construction details:			
$L_e = 2.03$ m, $L_c = 0.305$ m, $L_a = 0.610$ m			
$D_i = 12.7$ mm, $D_o = 22.2$ mm			
4 wraps of 40 screen mesh			
Artery Grooves:	Evaporator	Adiabatic	Condenser
No.	24	12	24
Width (mm)	0.79	2.38	0.79
Depth (mm)	1.4	2.38	2.38
Vapor vents:			
No./groove	24	117	42
Size (mm)	6 × 0.79	3 × 0.79	12.7 × 0.79
Axial slot spacing (mm)	6	6	1.5

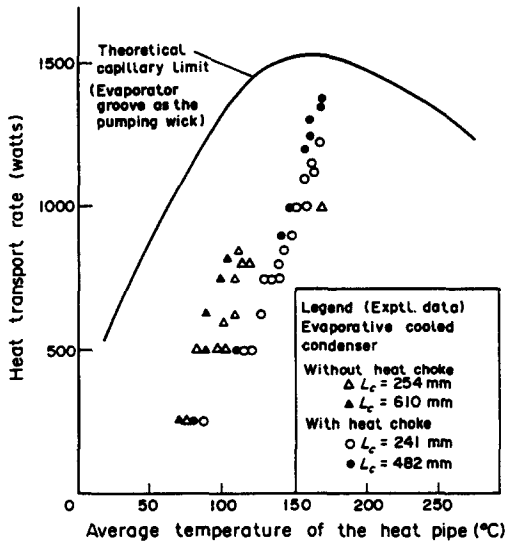


Fig. 16. Double wall artery heat pipe performance at zero tilt using water.
Copyright ©AIAA; reprinted with permission.

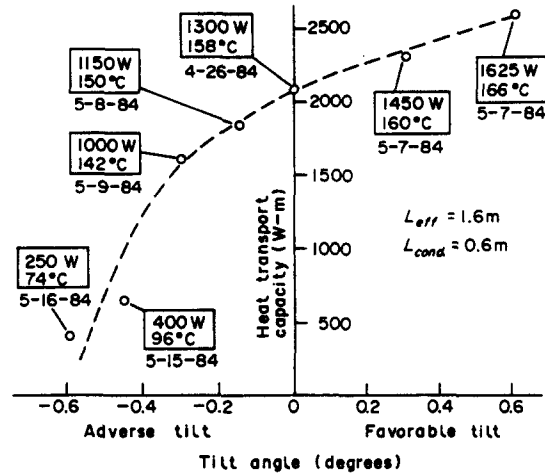


Fig. 17. Double wall artery heat pipe performance with tilt.
Copyright ©AIAA; reprinted with permission.

A concern about the reduced performance level led to the flow visualization studies in [8] with the outer tube of the heat pipe manufactured from glass to isolate possible problems associated with the artery groove depriming, condenser quenching effects, non-wetting of the wick with liquid, and vapor blockage of the liquid arterial channels. These performance tests were necessarily performed at low temperatures with the observation that the evaporator screen wick and narrower grooves of the condenser primed immediately with the liquid, while the larger grooves of the transport section did not fill completely. The heat input produced partial depriming and injection of vapor bubble into the liquid artery grooves, leading to a possible countercurrent flow of liquid and vapor in the transport section. This problem was cured by introducing a 5 cm long and 40 mesh size screen into the transport arteries close to the evaporator side to provide an axial resistance to vapor flow. This mesh insert appears to explain the previous loss of capillary pumping ability at the screen and evaporator groove interface. A change of the screen insert length to 1.27 cm and 24 mesh size did not affect the conclusions obtained with 5 cm and 40 mesh size, at least for the low temperature (20–120°C) water tests.

2.1.6. *High performance flexible heat pipes.* The flexible heat pipes use flexible screen arteries in the adiabatic or transport section with suitably integrated wick structures in the evaporator and condenser sections. [9] evaluates three different heat pipe configurations of the evaporator and condenser construction: (1) the circumferential “V” grooves; (2) multiple screen wraps; (3) the sintered powder metal wicks. These three wick configurations are integrated into an analytical model to determine the effect of individual wick geometry on the maximum heat transfer. The results from the “V” groove parametric study show that a 20° groove angle and 40–60 threads cm^{-1} give the highest throughput powers, while maintaining the requirement of the groove machinability. In addition, the spiral groove performance on the Earth degrades from an optimum pipe diameter between 0.95 cm and 1.59 cm. Table 4 shows the choices of the design parameters for each acetone–copper heat pipe configuration with each heat pipe being nominally the same except for the wick structure. The performance of each wick is shown in Table 5, whereas a comparison of the predicted performance with tests is summarized in Table 6. The results show that the powder metal wick heat pipe provides a lower temperature drop and larger radial power densities than other designs. Screen wicks have clearances between the individual screen layers and between the screen and the pipe wall which introduces a thermal resistance for heat transfer. The powder metal wicks in the evaporator and condenser produced radial power densities in excess of 8 W cm^{-2} . The researchers did not identify the highest heat load capability of the flexible heat pipe, which is the objective of their continuing development work.

Table 4. Flexible heat pipe construction details

Heat pipe material: copper
Working fluid: water
Construction details:
$L_e = 0.178$ m, $L_g = 0.381$ m, $L_c = 0.178$ m
$D_o = 16$ mm, Wall thickness = 1.27 mm
Wick geometry:
(A) Screen wick: 100 mesh, 2 wraps, 2 arteries of ss with 3.3 mm diameter each
(B) Powder metal wick: 325 mesh and 1.016 mm thick, 2 arteries of ss with 2.54 mm outside diameter
(C) Spiral "V" groove: 0.20 mm groove width and 0.55 mm depth, 51 grooves cm^{-1} , 2 arteries of ss with 3.3 mm outside diameter

Table 5. Flexible heat pipe calculated performance

Parameter	"V" groove	Screen	Powder metal
Max. load (W)	135	690	2350
Evap. temp. ($^{\circ}\text{C}$)	60	60	60
Radial power (W cm^{-2})	1.3	7	39
Temp. drop ($^{\circ}\text{C}$)	0.33	50	6
Thermal resist. ($^{\circ}\text{C W}^{-1}$)	0.0024	0.073	0.0026

Table 6. Comparison of the flexible heat pipe calculated and measured performance

Parameter	Screen		Powder metal	
	Calc.	Measured	Calc.	Measured
Load (W)	500	500	500	500
Evap. temp. ($^{\circ}\text{C}$)	60	79	60	75
Radial power (W cm^{-2})	5.2	5.2	8.3	8.3
Temp. drop ($^{\circ}\text{C}$)	36	43	5	13

2.1.7. *Dual pair artery liquid metal heat pipe.* Merrigan *et al.* [10] at the Los Alamos National Laboratory developed the dual pair artery liquid metal heat pipe with the geometry shown in Fig. 18 for the operation with lithium at about 1500 K. The 2 m long ($L_e = 0.3$ m and $L_c = 0.5$) heat pipe is made from molybdenum alloys (screen and body) and achieved an axial power density of 19 kW cm^{-2} at 1465 K with the corresponding evaporator radial flux of 150 W cm^{-2} . The heat pipe operated for 100 h at 15 kW and 1500 K without the degradation of performance [11].

2.1.8. *Heat pipes with modified wick structures.* Ismail, Liu and Murcia [12] studied the modification of the stainless steel mesh wick within heat pipes both analytically and experimentally for three different types of wick structures as depicted in Fig. 19. Using water as the heat pipe's working fluid shows that the wick geometry of Fig. 19a is 23.5 per cent more effective, whereas that of Fig. 19b is 34 per cent more effective than the usual uniform wick design (wick without modifications). The steady state model results also agree well with the data.

2.1.9. *Heat pipes with wicks made of sintered metal powders.* The sintered metal powder or fiber wicks, when combined with separate radial and axial liquid and vapor flow channels, can greatly improve the heat pipe performance. [13] reports on the development of a heat pipe with a sintered

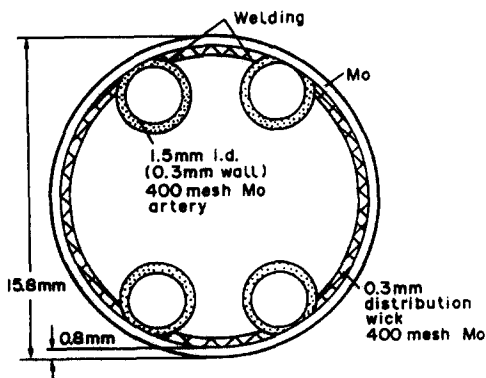


Fig. 18. Dual-pair artery liquid metal heat pipe configuration.

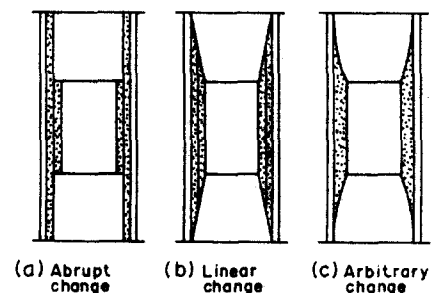


Fig. 19. Heat pipes with wick modifications.

Table 7. Properties of the metal powder wicks for the effective conductivity tests
Copyright ©AIAA; reprinted with permission

Wick	Mesh range	Permeability (cm ²)	Pore radius (cm)	Porosity (%)
Ni 200	60/80	1.2×10^{-7}	0.0034	69
Ni 200	80/150	1.5×10^{-7}	0.0034	43
Ni 200	250/325	2.0×10^{-7}	0.0035	64
Cu C102	100/170	9.3×10^{-8}	0.0036	59
Cu C102	170/200	5.5×10^{-8}	0.0037	52
Cu C102	325/—	1.2×10^{-9}	0.0033	32

bronze wick integrated into the inside of the tube wall. When comparing the performance of this heat pipe with a water heat pipe using a sandwich of 50 and 100 mesh screens in combination, the sintered metal heat pipe gives a superior performance which, as in the discussion of the flexible heat pipes above, is attributed to the reduced thermal resistance between the wick and pipe wall. The manufacturing process of sintered metal heat pipes is also more than 50 per cent less expensive than for the conventional heat pipes.

Peterson and Fletcher [14] investigated the effective thermal conductivity of sintered nickel and copper powders from 25–100°C for several different porosities in dry and saturated water conditions. Table 7 shows the wick samples tested and Figs 20 and 21 illustrate the experimental data. These data show: (1) that the effective thermal conductivity, k_{eff} , of the sintered copper is much larger than that of the sintered nickel for dry and wet powders; (2) that the effective thermal conductivity increases slightly with temperature; (3) that k_{eff} for the wet sintered metal powder is greater than that for the dry sintered powder. In general, the effective thermal conductivity of sintered metal powders is a function of the metal from which the powder is made, thermal conductivity of the fluid filling the pores, the powder porosity and the mean temperature of the sintered metal wick structure.

2.1.10. *Ceramic heat pipe.* Merrigan and Keddy [15] describe the development of a ceramic heat pipe with the capability of operation above 1200 K in air and combustion product environments. They envisaged using this heat pipe in the industrial waste heat recuperators with corrosive waste gases and high temperatures, using sodium or lithium as the working fluids. As sodium and lithium are not compatible with the ceramic material, this material must be suitably protected, such as by using a Chemical Vapor Deposition (CVD) process to line the interior of the ceramic tube with a layer of refractory metal as shown in Fig. 22. A circumferential wick may be incorporated as a separate structure or as a part of the metallic liner. The ceramic tube/refractory metal liner materials must satisfy the requirements of strength, chemical stability, resistance to thermal shocks, fabricability and the capability of being joined with vacuum tight joints.

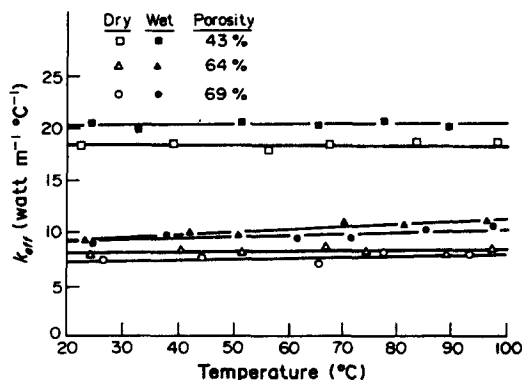


Fig. 20. Thermal conductivity variation with temperature and porosity for the sintered nickel powder wick.
Copyright ©AIAA; reprinted with permission.

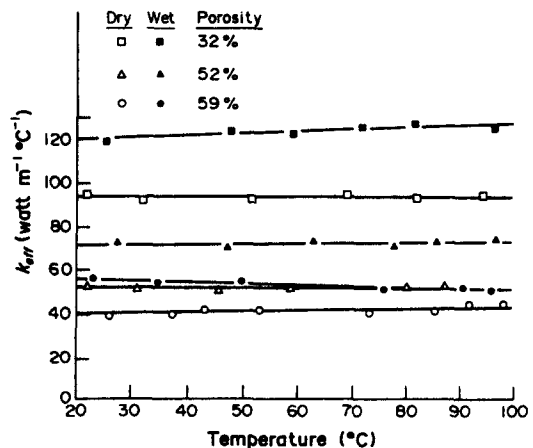


Fig. 21. Thermal conductivity variation with temperature and porosity for the sintered copper powder wick.
Copyright ©AIAA; reprinted with permission.

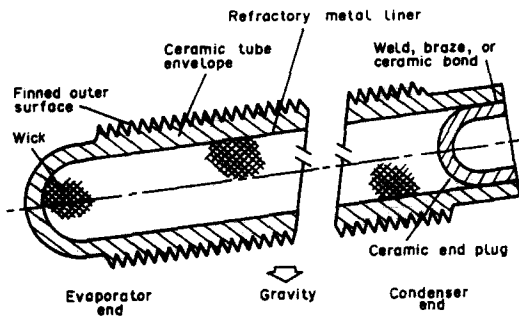


Fig. 22. Ceramic heat pipe configuration.

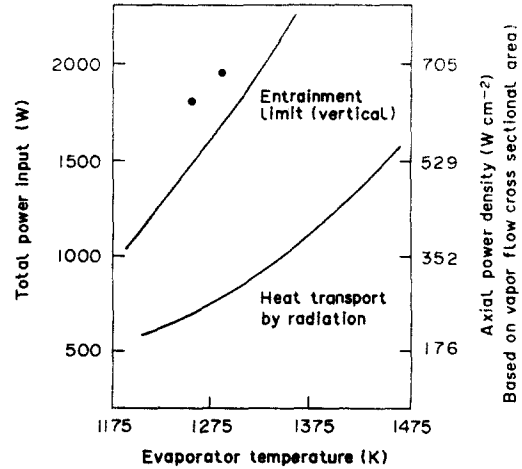


Fig. 23. Performance of the ceramic heat pipe.

Investigations showed that the primary candidate materials satisfying the above requirements with the working fluid sodium, are silicon carbide (the heat pipe ceramic material) and tungsten (the metal liner). The construction of the ceramic heat pipe involved the fabrication of CVD tubes of $L_e = 0.61$ m, $D_0 = 25$ mm and 0.3 mm wall thickness and then lining them with CVD tungsten (0.1–0.3 mm thickness), which served as the wick material.

The performance tests of the ceramic heat pipes were conducted in a vacuum furnace at 1200 K. Figure 23 shows the test data with a 0.2 m heat input zone of the pipe and illustrated entrainment limiting heat fluxes generated by a model of a wickless heat pipe. The demonstrated heat flux of 1.96 kW at 1010 K with the corresponding axial heat flux of 692 W cm^{-2} is not an absolute limit. The SiC heat pipe underwent 34 starts from room temperature to temperatures greater than 1200 K, and was operated for more than 200 h above this temperature.

2.1.11. *An enhanced boiling surface thermosyphon.* Larkin [16] recently studied the enhancement of heat transfer in a water/copper thermosyphon using the following enhancement methods at the inside surface of the evaporator: (1) copper mesh; (2) copper sleeve inserts with re-entrant cavities; (3) a teflon sleeve; (4) a teflon sleeve with a recess to trap the fluid. At temperatures above 50°C the data with different enhancement methods show no enhancement in the heat transfer, whereas at lower temperatures they show that enhancement of heat transfer of up to 200 per cent may be achieved with a copper mesh extending the full length of the evaporator.

2.2. Transient heat pipe studies

The objectives of recent transient experimental and analytical studies have been to understand the transient heat pipe response and to develop modeling capabilities of this response for the variable and step input heat loadings at the evaporator and condenser surfaces. The transient heat pipe response is dictated by the thermal capacity of the heat pipe shell, capillary structure, working fluid, liquid and vapor dynamics, and on the mode of heat transfer to the evaporator and withdrawal from the condenser.

Based on the experimental observations in a Freon-11 heat pipe, Colwell and Chang [17] classified the transient heat pipe operation into four modes: (1) the heat transfer is modest and so the heat pipe smoothly and easily accommodates the external changes on the heated and cooled surfaces with the capillaries being fully wetted; (2) the heat transfer is such that a portion of the capillary structure in the heated zone dries and large internal temperature variations occur, but the heat pipe nevertheless reaches a steady state operation after a certain time; (3) the heat pipe fails completely as a result of the excessive heat transfer rates; (4) a start-up from the thermodynamic supercritical state (as in the cryogenic heat pipes) which requires at first bringing the working fluid into a two-phase mixture region, or a start-up from a frozen fluid state where the working fluid must first be melted and vaporized to start the normal heat pipe operation.

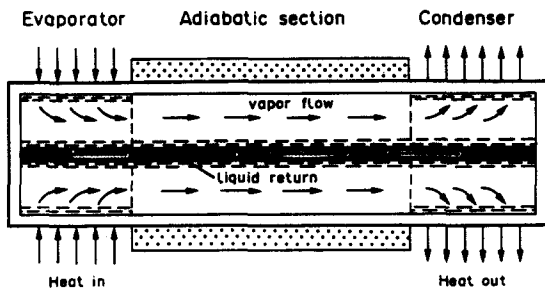


Fig. 24. Heat pipe configuration of Colwell and Chang (1984).

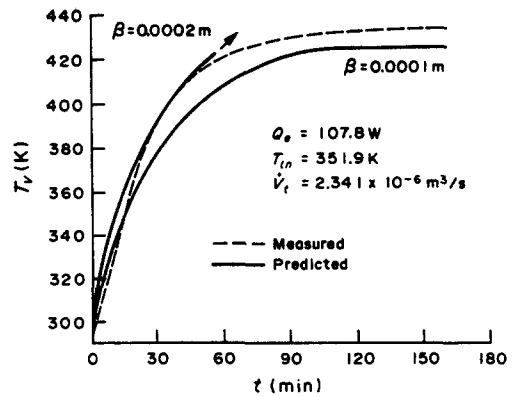


Fig. 25. Transient heat pipe response of Colwell and Chang (1984).

Working fluids with high vapor densities (water, ammonia, methanol) when started from the room temperature, attain a uniform start-up rate because of the establishment of the fast working fluid circulation. When the vapor densities of working fluids are low (sodium, lithium) and the temperature of the medium surrounding the heat pipe is also low, such that the molecular free path of the vapor exceeds the vapor channel diameter, the start-up becomes frontal [19]. The heat transfer close to the evaporator end will then primarily be determined by convection and close to the condenser end by conduction, with the two separating zones possessing a clearly defined frontal region.

Figure 24 illustrates the heat pipe used in the transient experimental and analytical studies of Colwell and Chang [17, 18]. They constructed this heat pipe from 316 ss (stainless steel) with $L_e = 0.8$ m, $D_o = 19.1$ mm, $D_i = 15.7$ mm, $L_a = 0.1524$ m, $L_c = 0.243$ m, a wick of ss and 100 mesh screen lined on the inside pipe wall of the evaporator and condenser surfaces, and with a central core slab that runs the entire length of the pipe. This slab consisted of 40 mesh size screen and was covered with two layers of 100 mesh screen. The working fluid used was Freon-11. The transient heat pipe behavior at various levels of the heat input was already noted above. In addition, high rates of heat transfer led to complete evaporator dryouts with the pressure and temperature of the fluid increasing and becoming very erratic close to the thermodynamic critical point. After the heat pipe restart at high pressure and temperature, very long periods of time (hours) were observed before the resumption of the normal operating conditions. On restarting the heat pipe with high values of the inlet coolant temperatures very long restart times occurred, even with the absence of heat transfer to the evaporator.

The work of Chang and Colwell [18] describes the analytical modeling of the heat pipe in [17]. This modeling involves: (1) the two-dimensional conduction in the pipe wall and circumferential wicks; (2) a one-dimensional lumped parameter modeling of the vapor core and the central composite wick for conditions below the critical temperature; (3) a one-dimensional modeling with phase change at the liquid front in the slab when the pipe is cooled from above the critical temperature. The effective heat capacity of the heat pipe involves the properties of the vapor and central wick slab and is modeled by accounting for the slab porosity and mesh screen thicknesses. The model neglects the thermal resistance at the liquid-vapor interfaces and includes various options for the boundary conditions at the evaporator and condenser. The numerical solution of the model equations and comparison of results with data [17] shows that the vapor temperatures agree well with each other for heat loadings below the dryout heat fluxes, for both the increasing and decreasing step changes of the input heat fluxes. At high heat loadings, however, the predicted vapor temperature distribution in the heat pipe depends on the assumed width or gap thickness β between the circumferential mesh screen layers, since large values of these gaps produce larger thermal resistances for heat flow and earlier times during which the vapor temperature begins to increase very rapidly, as shown in Fig. 25. By incorporating a dryout model within the analysis (which they did not do), this vapor temperature increase would be associated with the dryout condition in the evaporator.

Beam [19] presents a simple lumped parameter model of the heat pipe's vapor core and compares the predicted results with data obtained in a heat pipe made of copper, four wrap screens of 100 mesh, $D_o = 22.28$ mm, $D_i = 19$ mm, $L_i = 0.457$ m, $L_e = 0.102$ m, $L_c = 0.355$ m and utilizing water as the working fluid. The equations used are of the following simple form:

$$Q_i = mCp \frac{d(T - T_{amb})}{dt} + \bar{h}A_c(T - T_{amb}) \quad (1)$$

$$T - T_{amb} = 0 \quad \text{at} \quad t = 0, \quad (2)$$

which upon integration yields.

$$T - T_{amb} = \frac{Q_i}{\bar{h}A_c} [1 - \exp(-\alpha t)], \quad (3)$$

where

$$\alpha^{-1} = \frac{mCp}{\bar{h}A_c} \quad (4)$$

is the time constant. For a given heat pipe, α^{-1} may be determined from a plot of the cool down temperature as a function of time and $\bar{h}A_c$ from the steady state data.

Comparisons of the predicted vapor temperature distribution with data agree well at low input powers. With large input starting powers, however, the predicted vapor temperature during the first few seconds of the transient do not compare favorably with the data which may be attributed to the partial drying in the evaporator, with a consequent rewetting of the wick. Beam tested this hypothesis with the development of a wick hydrodynamic model to be used in addition to the above equations. The final model is characterized, therefore, by a thermal response period of the vapor and a hydrodynamic response period of the wick with the solution properties as given in [20] for the heat pipe in [19]. Figure 26 illustrates the predicted liquid front interface location with time for different step power inputs. With an increase in this power, the liquid front in the wick recedes, at first towards the condenser but soon thereafter it changes direction, due to the increased effect of capillary pumping at higher temperatures, and complete rewetting of the wick occurs. However, when the heat input is sufficiently large (225 W in Fig. 26) no rewetting of the wick results. This theoretically predicted process of liquid front motion with time agrees with data of the pipe wall temperature measurements with time at the beginning and end sections of the evaporator as shown in Fig. 27. (Note, however, that in the experiment at 225 W no runaway dryout in the evaporator occurred as predicted by the model.)

Reference 21 describes an Advanced Simulation and Analysis of Heat Pipes (ASAHP) computer program for the transient analysis of heat pipes. The program is interactive and incorporated within

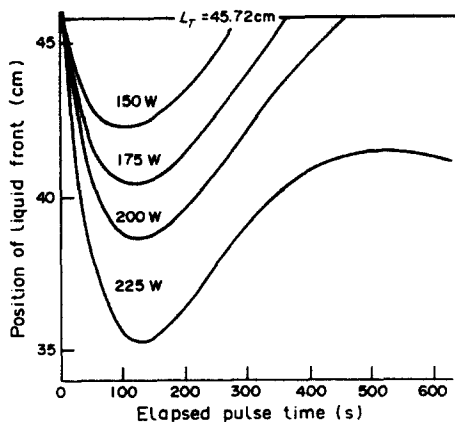


Fig. 26. Predicted liquid front motion [Ambrose, Chow and Beam (1986)].

Copyright ©AIAA; reprinted with permission.

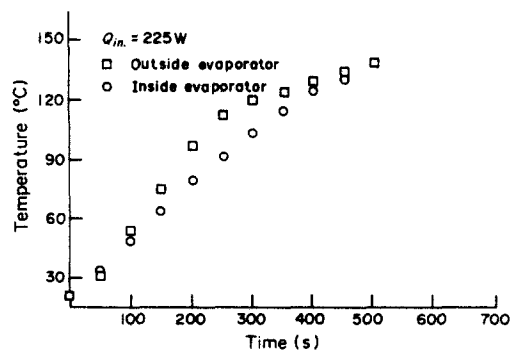


Fig. 27. Measured evaporator temperatures [Ambrose, Chow and Beam (1986)].

Copyright ©AIAA; reprinted with permission.

Table 8. Current and planned ASAHP capabilities
Copyright ©AIAA; reprinted with permission

Area	Feature	Current	Planned	
Pipe types:	Axially grooved	X		
	Homogeneous wall wick	X		
	Internal artery	X		
	Other designs		X	
Fluids:	Refrigerants at T_{room}	X		
	Liquid metals	X		
	Cryogenics		X	
Models:	1-D and 2-D	X		
	Pressure recovery	X		
	Reversibility	X		
	Tilt	X		
	Condenser back pumping	X		
	Condenser flooding	X		
	Liquid/vapor shear	X		
	Noncondensable gases		X	
	Heat transfer:	3-D conduction	X	
		Coefficient correlation	X	
Temperature recovery			X	
Off-design:	Wicking limit simulation	X		
	Entrainment limit simulation	X		
	Boiling limit flagging	X		
	Boiling limit simulation		X	
	Sonic limit flagging	X		
	Sonic limit simulation		X	
	Freeze/thaw simulation	X		

a thermal network analyzer that allows the user to define the heat pipe characteristics. Table 8 provides a summary of the current and planned ASAHP capabilities with the computer program currently running on IBM PC compatible microcomputers. To date only the steady state comparisons of the program's predictions with data have been made with good results [21].

Tilton, Chow and Mahefkey [22] investigated the transient response of a sodium heat pipe both analytically and experimentally with the heat pipe characteristics: $L_i = 0.457$ m, $L_c = 0.305$ m, $L_e = 0.152$ m, $D_o = 12.7$ mm, $D_i = 10.3$ mm, $D_v = 10.62$ mm, shell and wick mass of 208.0 g, sodium mass of 8.0 g, and inconel 617 screen with 100 mesh size having a wick permeability of 4.2×10^{-10} m². The analytical modeling involved the development of a distributed lumped parameter model, where the heat pipe is divided into a number of sections and transient mass conservation and energy balances are written for each section. Tilton *et al.* used the lumped parameter form of the momentum equation for each section to relate the vapor pressure gradient to the vapor friction and change of the mass flux. To close the governing differential equations they used the Clausius-Clapeyron equation and constitutive equations for the vapor friction and effective thermal capacity. The model also incorporates the capillary wicking limit heat flux for the prediction of dryout. Comparison of the model predictions with the transient data of the pipe wall temperature distributions at various heat flux loadings are reasonable, but not too accurate because of the model's neglect of the heat pipe's shell and wick thermal resistances. Nevertheless, the developed model is useful for studying internal heat pipe processes of condensation, evaporation and dryout.

The life testing of a sodium inconel 600 heat pipe [23] shows that it can fail due to the corrosion and impurities in the sodium. The heat pipe also exhibited a degraded performance, measured in terms of the temperature increase with time between the evaporator and condenser. The heat pipe failure modes were determined on the basis of the microscopic examinations of the heat pipe surface after extended operations at temperatures in excess of 990 K.

The temperature control of various power dissipating systems can be accomplished by the Variable Conductance Heat Pipes (VCHP). To provide modeling capabilities of these heat pipes Bobco [24, 25] recently developed a lumped parameter model for the VCHP geometry as illustrated in Fig. 28a. The basic modeling equations involve: (1) a fin equation (local conservation of energy relating the axial conduction in the pipe wall and wick, radial condensation and radial heat loss to the ambient); (2) a heat balance equation relating the heat power entering the evaporator to that lost by condensation to the inner pipe surface; (3) a noncondensable gas mass balance equation relating the position of the condensation front to the mean density of gas in several pipe zones

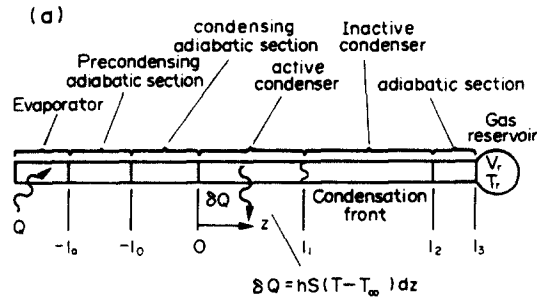


Fig. 28a. Schematic of the VCHP used for the model of Bobco (1987).
Copyright ©AIAA; reprinted with permission.

and the gas reservoir; (4) the pressure/temperature correlation for the saturated vapor of the working fluid. With the assumption of no axial conduction at the evaporator/primary adiabatic zone interface, temperature matching at zone boundaries and heat loss at the reservoir/condenser interface, the governing equations were solved for the heat pipe temperature distribution and condensation front location as a function of heat load, environmental conditions and fluid properties. Bobco accomplished the model verification with data using heat loads from 0–100% for two different heat pipe geometries and working fluids as shown in Table 9. Referring to Fig. 28b, the significant conclusions from modeling are: (1) for very low heat loads, the condensation front occurs in the primary adiabatic region; (2) for moderate to full heat loads, the condensation front occurs in the mid to far section of the condenser, and the performance is dominated by the heat loss from the condenser section; (3) for low to moderate heat loads the condensation front occurs in the near to mid-section of the condenser, and the performance depends on heat losses from the primary adiabatic and condenser sections; (4) the role of heat leaks must be recognized in the analysis.

In the modeling effort of VCHP discussed above, the author assumes the diffusion region between the working fluid vapor and the noncondensable gas to be of negligible thickness. For terrestrial applications with the evaporator below the condenser and with the noncondensable gas of a lower molecular weight than that of the working fluid, this assumption is reasonable. When the noncondensable gas has a higher molecular weight than that of the working fluid, however, the gravity may play a significant role on the definition of the gas/vapor diffusion region in a heat pipe. Kelleher [27] reports on the development of a one-dimensional model to predict this effect of gravity on the operation of a vertically oriented VCHP. He claims to obtain good comparisons between the model predictions with data for a wide range of heat pipe operating conditions for both situations of noncondensable gas of lower (helium and methanol) and higher (krypton and methanol) molecular weights than that of the working fluid.

Table 9. Heat pipe designs used for verification of variable conductance model of Bobco (1987)

Heat pipe:	Edwards & Marcus (1972)	Bobco (1987)
Working fluid:	water	ammonia
Inert gas:	air	nitrogen
Pipe:		
Material	stainless steel	aluminum
Outer diameter (mm)	14.4	12.7
Wall thickness (mm)	0.914	0.711
Overall length, (m)	1.39	2.03
Condenser length (m)	0.768	0.641
Evaporator length (m)	0.318	0.521
Wick structure:		
Material	200 mesh	A1 core knitted
Description	Concentric annulus artery (0.39 mm gap width) with 2 wraps of screen	mesh or wall 120 mesh of ss
Gas reservoir:	—	252 cm ³
Bends:	—	80 and 74 degrees

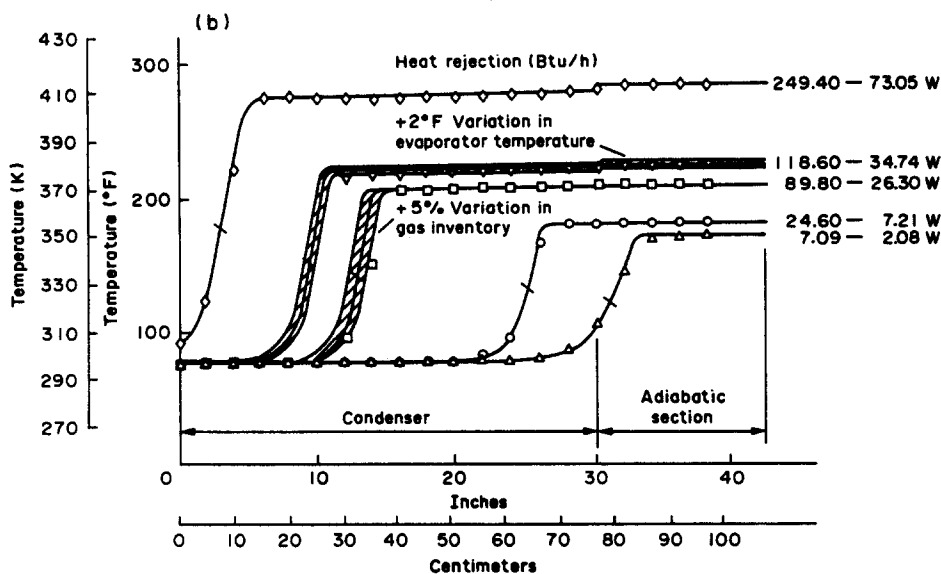


Fig. 28b. Comparison of the measured and predicted VCHP temperature profiles, Bobco (1987). Copyright ©AIAA; reprinted with permission.

2.3. Gravity assisted heat pipes or thermosyphons

The gravity assisted heat pipe or thermosyphon research continues to be a lively field of investigation, primarily because of its simple construction, a capability to transfer large heat fluxes and interesting limiting operational modes. Fukano *et al.* [28, 29] experimentally studied the thermosyphon's limiting operational behavior using water and methanol as the working fluids and different tube diameters and liquid fillings. They observed that increasing the heat transfer to the evaporator at the bottom of the thermosyphon causes more and more liquid to be evaporated from the liquid pool until the upflowing vapor produces an instability of the downflowing liquid film at the liquid-vapor interface leading to the entrainment of liquid in the vapor and thinning of the film. This state may be associated with the dry patch formation just above the top of the liquid pool (Fig. 29a). This dry patch then grows (Fig. 29b) with the simultaneous increase in the evaporator wall temperatures (E1-E5), but with a reduction in the vapor pressure (P) caused by the reduced vapor generation rate owing to the reduced wetted wall area until the upflowing vapor can no longer sustain the flooding condition. At this point (Fig. 29c), the liquid accumulated in the condenser falls into the pool in the evaporator (deflooding) and the falling liquid hits the hot evaporator surface and film boils (Fig. 29d) and cools the wall through a vapor layer. With the vapor generation rate now exceeding the condensation rate, the system pressure increases from (c)-(d) and eventually it decreases as a result of the heated wall cooling. When the flooding condition is satisfied again, the cycle is repeated producing an oscillatory system operation. Fukano *et al.* observed these "flooding triggered" flow oscillations of about one third for liquid fillings and large tube diameters and classified them as TYPE I (Fig. 30) on the flow map. TYPE II labeled points in Fig. 30 correspond to small tube diameters and are associated with the thermosyphon operation leading to a different steady state at a lower pressure, whereas the TYPE III data points are associated with a switch to a steady state at a higher pressure. Types II and III operating modes are thus nonoscillatory, but represent a switch to different flow regimes.

The analytical modeling of some limited thermosyphon behavior is described in [30]-[32]. Dobran [30] proposed a lumped parameter model for the analysis of transient thermosyphon behavior by deriving the differential equations for the average liquid film thickness, film temperature and pool height, and studied the thermosyphon operational characteristics in terms of the independent parameters characterized by its geometry, liquid filling and fluid's thermophysical property groups. Figure 31 presents some steady state results for the heat input Q_i^* vs the film thickness $\bar{\delta}$ for different values of the two-phase Grashof number parameter N_L , liquid filling h^*/l^* and fixed values of the capillary number Ca , density ratio $\rho^* = \rho_v/\rho_l$, viscosity ratio

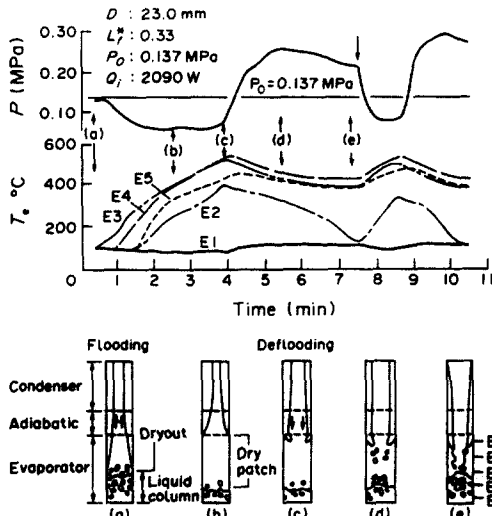


Fig. 29. Observed thermosyphon flow oscillations.

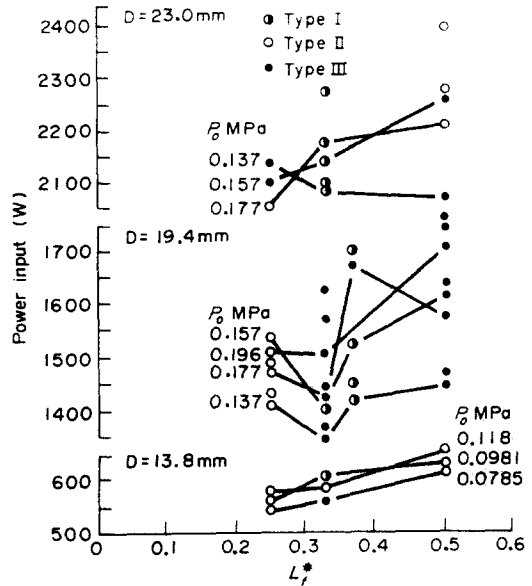


Fig. 30. Thermosyphon flow regime stability map.

$\mu^* = \mu_v/\mu_l$ and $l^* = L/R$. The linearized analysis of [30] and nonlinear analysis of [31] demonstrate that at low liquid fillings there is a one to one correspondence between the heat input and steady state solution, and that the solution is stable until the liquid pool dries out (point A in Fig. 31, for example). For large liquid fillings h^*/l^* , there are two possible steady state solutions for each heat input, with one being stable (point D) and the other being unstable (point D'). The exchange of stabilities occurs at the turning point C and can be associated with the entrainment limiting operation by comparing the predicted heat fluxes with data [30].

Reed and Tien [32] extended the basic thermosyphon modeling approach proposed by Dobran [30] by further dividing the liquid film and vapor core into three separate sections, with each section in the condenser, adiabatic and evaporator regions having average properties. Complementing the resulting distributed lumped parameter model by the appropriate laminar and turbulent expressions for the constitutive equations of heat and mass transfer in each region, has the potential of predicting the film thickness, mass fluxes, vapor and liquid temperatures, liquid pool height, and the dryout and flooding operating limits. The dryout limit may be predicted when either the liquid pool dries out or when the liquid mass flow rate at the liquid pool level is reduced to zero. The flooding limit occurs when the rate of change of the film thickness with respect to the heat input becomes unbounded (point C in Fig. 31). A comparison of the steady state results for the film thickness in the adiabatic region vs the film Reynolds number, and the film Reynolds number vs the vapor temperature at the onset of flooding with the data of [32, 33] produced very good results as may be seen in Figs 32 and 33. Reed and Tien [32] also carried out a nonlinear analysis of the transient system of equations, but the lack of transient data has precluded the model verification.

In thermosyphons with the noncondensable gas the vapor carries the gas into the condenser where it is trapped. The diffusion, convective mixing and buoyancy between the gas and vapor control the distribution of gas in the condenser. Hijikata [34] developed a model of this gas-vapor distribution by neglecting the convective mixing and buoyancy effects and calculated the two-dimensional gas and vapor distribution profiles. The parametric study on the radial diffusion shows that this diffusion is affected by the gas load and the ratio of the radial gas diffusion rate to the condensation rate parameters. When these parameters are small, the radial diffusion becomes pronounced and the one-dimensional diffusion front model becomes inadequate. Using a recently developed miniature wet bulb/dry bulb probe in a test thermosyphon with water and helium, Peterson and Tien [35] measured the radial and axial concentration profiles and used these data to verify the model predictions [34] at different input power levels. This comparison shows good agreements in experiments with minimal buoyancy effects. When the buoyancy effects are significant, however, the gas concentration profile has a flatter distribution across the thermo-

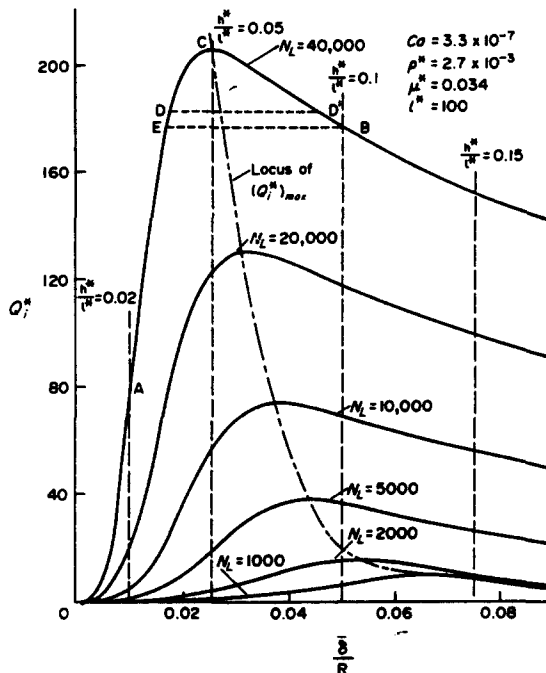


Fig. 31. Predicted thermosyphon steady state characteristics, Dobran (1985).

syphon diameter than the analysis can predict, indicating that the future analytical modeling should appropriately account for the buoyancy and convective mixing.

Large axial heat fluxes in a thermosyphon produce an entrainment limiting operation and thick condensate film because of the presence of waves on the liquid film-vapor core interface. A unidirectional thermosyphon, as illustrated in Fig. 34, eliminates the countercurrent flow limiting operation and it should produce thinner liquid films which should allow for larger heat transfer rates. The research reported in [36] had the objective of ascertaining these claims experimentally with two different fluids, ethanol and water. The tests show that: (1) a unidirectional flow is possible with the design as shown in the figure; (2) the unidirectional flow produces 10% thinner films than in a conventional thermosyphon with equivalent diameter, evaporator length, adiabatic length, condenser length and working fluid; (3) higher heat fluxes and operating limits exist in a unidirectional heat pipe; (4) the unidirectional heat pipe exhibits larger and more erratic start-up transient periods than the conventional thermosyphon. The last conclusion is clearly a disadvantage and more research is needed to quantify it.

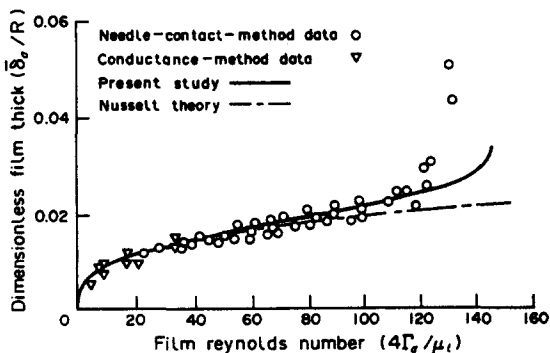


Fig. 32. Comparison of the predicted with measured thermosyphon film thickness with film Reynolds number, Reed and Tien (1987).

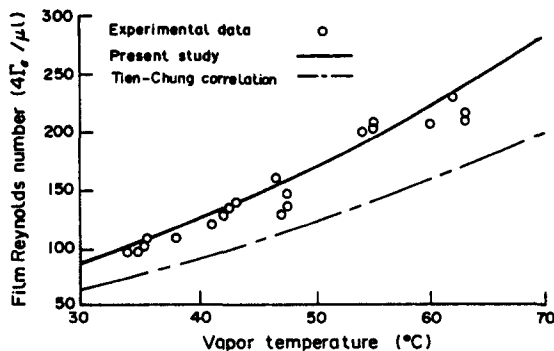


Fig. 33. Comparison of the predicted with measured thermosyphon film Reynolds number with vapour temperature at flooding, Reed and Tien.

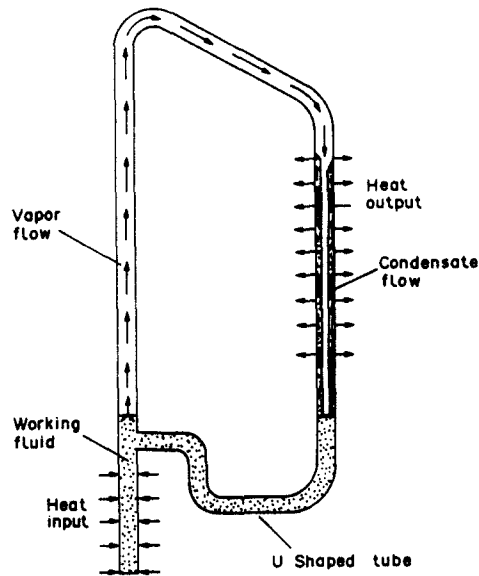


Fig. 34. Unidirectional thermosyphon.

2.4. Rotating heat pipes

Reference [37] reports on the measurements of film heat transfer coefficients in a cylindrical, co-axial rotating heat pipe with a stepped condenser section at rotational speeds of 700, 1400 and 2800 rpm using water as the working fluid. The active condenser had a length of 0.25 m and three different diameters. The condenser performance increases with the rotational speed and diameter, and with an inserted tube yields from 1.3 to 1.5, an improvement of performance at each rotational speed over that without the insert. Comparing the experimental data with the laminar and turbulent condensation models with the gravitational body force replaced by the centrifugal acceleration force, the data exhibit a more complex behavior than the models can predict.

2.5. Miscellaneous heat pipe operational studies

Silverstein [38] developed heat transfer correlations for the sonic, entrainment and boiling limits as power law functions of the vapor pressure for lithium, sodium, ammonia, and Freon-11 from 1 to 100 psia.

In the evaporator and condenser sections of a heat pipe the velocity profiles deviate considerably from the developed laminar and turbulent pipe flow. High heat fluxes produce high radial Reynolds numbers of the vapor and yield a turbulent flow in cylindrical condensers even if the axial Reynolds number is below 2000. Haug and Busse [39] performed experiments on the pressure recovery in a cylindrical heat pipe for the radial Reynolds number range $5 < Re_r < 150$ and axial Mach number range $0.1 < Ma < 1$. The vertical, gravity assisted heat pipe used for this purpose consisted of aluminum with longitudinal grooves using dodecane as the working fluid (to attain high values of Re_r and Ma), operating from 25 to 55°C with power levels of 15–450 W and condenser observational windows. To reduce the flow fluctuations and liquid accumulation in the condenser at high Mach numbers, the heat pipe was designed to suppress these effects and the static pressure was measured at the beginning of evaporator, middle of the adiabatic and at the end of the condenser regions. The pressure recovery data show a strong recovery in subsonic flow and a decrease in recovery when the local Mach number in the core becomes supersonic. The higher the operating pressure of the heat pipe, the higher the radial Reynolds number becomes at which the supersonic flow occurs. The pressure recovery becomes 50% at $Re_r \approx 5$ and 93% at $Re_r \approx 50$, and remains at 93% for $50 < Re_r < 150$. The analysis of the pressure recovery was performed with the model developed in [40], which uses a laminar two-dimensional model and a turbulent one-dimensional model to describe the compressible vapor flow in heat pipes. For $Re_r < 30$, the laminar model

calculations agree best with data, whereas for $Re_v > 80$ the turbulent model calculations better reproduce the experimental pressure recovery trend.

Mechanical roughening of the heat pipe's inner wall is effective in inhibiting the liquid-vapor interaction in vertical thermosyphons. The experiments conducted with potassium as the working fluid in three different heat pipes with knurled internal walls (0.51 mm, 0.38 mm and 0.20 mm) are described in [41]. The tests had the objective of validating an entrainment limiting heat flux correlation previously validated for sodium, mercury, water, acetone, and toluene (Ref. 4 in [41]). This entrainment limiting heat flux due to knurling is given as:

$$\frac{Q}{A_v} = \frac{(2\pi)^{0.5}}{\delta^*} h_k (\sigma \rho_v \delta)^{0.5}, \quad (5)$$

where A_v is the vapor flow area, $\delta^* = 0.074$ cm is the reference length and δ is the depth of surface texturing (knurl depth in cm). Comparing the predicted limiting heat fluxes using equation (5) with the potassium data reveals that the impurities in potassium produce lower limiting heat flux values and that a distillation of potassium into the heat pipe produces results much closer to the predicted ones. A theoretical result is also suggested in the paper for the minimum depth of surface texturing:

$$\delta_m = \delta^* \left[\frac{(\rho_l - \rho_v)g}{\sigma} \right]^{0.5} \quad (6)$$

on the inside of the pipe for an improvement in heat pipe performance over the corresponding smooth-walled case. For potassium at 500°C, $\delta_m = 0.016$ cm.

The Marangoni effect or the surface tension variation with temperature may play a significant role in the heat pipe performance. Kosson and Harwell [42] studied this for an axially grooved VCHP and compared the results with the ammonia-nitrogen data. The analytical results predict a substantial reduction in the heat transfer capacity because of the Marangoni effect and compare favorably with the limited experimental data.

3. HEAT PIPES IN TERRESTRIAL APPLICATIONS

3.1. Heat recovery systems

The use of heat pipes in heat recovery systems has the potential of increasing the heat transfer efficiency when used as heat exchange devices and reducing the systems cost owing to their low maintenance cost. The use of a ceramic heat pipe [15] for the operation in high temperature industrial waste heat recuperation was discussed previously in Section 2. Another application is in petroleum refineries where they use heat pipes in combustion air preheaters, waste recovery boiler and process fluid coolers [43]. Here the heat pipes are designed to operate in the gas temperature from 500 to 1000 K and with $D_o = 51$ mm. They are made of carbon steel with spiral fins 19 mm high, 1.3 mm thick, 0.24 fins mm^{-1} (clean gas), 0.12–0.16 fins mm^{-1} (no. 6 oil) and 0.08–0.12 fins mm^{-1} (gas with abrasive particulates). For maximum heat transfer efficiency, the heat pipe arrangement must be staggered. Other applications to heat recovery systems appear in [44–49].

3.2. Rankine and solar systems

Chuah and Kreith [50] discuss an interesting heat pipe Rankine engine in which a turbine is placed into the vapor flowing between the evaporator and condenser of a heat pipe (Fig. 35) and a mechanical pump used as an aid to return the condensate into the evaporator. With Freon-11, Freon-12, ammonia, water and carbon tetrafluoride as working fluids operating at modest temperatures, the proposed concept can apparently achieve an efficiency of 15%. For a 1 KW power output, calculations showed that the heat pipe diameter would have to be about 8 cm and wick thickness 1 cm.

Foster and Kowalski [51] describe a heat pipe collector concept for water heating using the thermosyphon principle, where the evaporator is coupled to a solar collector and the condenser to the solar storage tank. They also describe the system analysis and comparison with the Freon-12 tests. Another solar energy application [52] involves a parabolic mirror to concentrate the solar energy on a heat pipe evaporator for the purpose of generating steam. The heat pipe evaporator is enclosed within a glass tube envelope 1 m long and 5 cm in diameter. The condenser section is

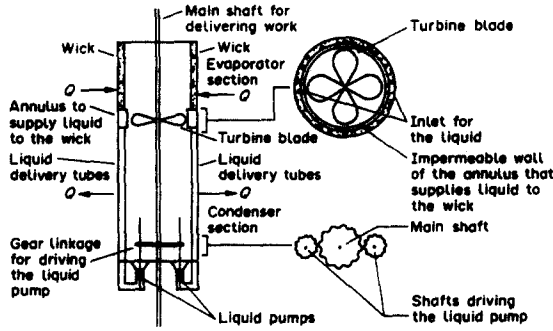


Fig. 35. Heat pipe Rankine engine.

0.4 m long and the heat pipe diameter is 2.5 cm with water used as the working fluid and a wick formed of a sandwich of three layers of screen, two layers with 54 and one layer with a 100 mesh screen. The proposed steam generating plant is composed of six units of concentrating collectors with an area of 2 m² each, an integrated condenser, a storage tank and other necessary plumbing.

3.3. Fusion reactor and high energy beam detector target cooling

Schwartz and Hoffman [53] consider the use of sodium heat pipes for the cooling of a lithium pool in the blanket surrounding the central cell plasma of a tandem mirror fusion reactor (schematically illustrated in Fig. 36). With the lithium pool temperature being from 1400 to 1500 K, considerations are given to the heat pipe arrangement and performance limits in a magnetic field, and to the liquid condensate return in the heat pipes, as this must flow perpendicularly to the magnetic fields (about 2 Tesla) for the heat pipes to remove the reactor heat from all radial zones. Strong magnetic fields produce induced eddy currents in the liquid yielding a reduction in the heat pipe's heat transport capacity as a result of the magnetic field's pressure drop, i.e.

$$\left(\frac{dP}{dz}\right)_B = \frac{\mu_l m_l}{\rho_l A_l w_h^2} \frac{H^2 C}{1 + C} \tag{7}$$

$$H = B w_h (\sum_l / \mu_l)^{0.5} \text{ (Hartmann number)} \tag{8}$$

$$C = \frac{\sum_w \delta_w}{\sum_l w_h} \tag{9}$$

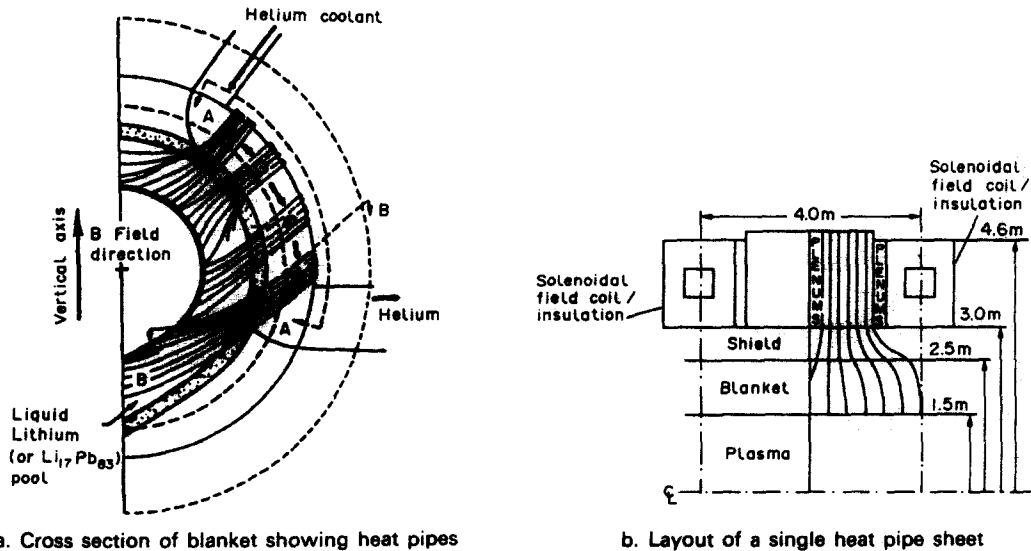


Fig. 36. View of a fusion reactor concept with sodium heat pipes used for lithium cooling.

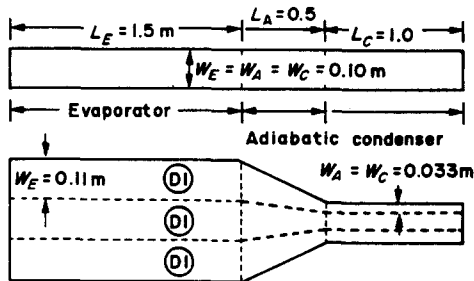


Fig. 37. Sodium heat pipe geometry for the fusion reactor cooling.

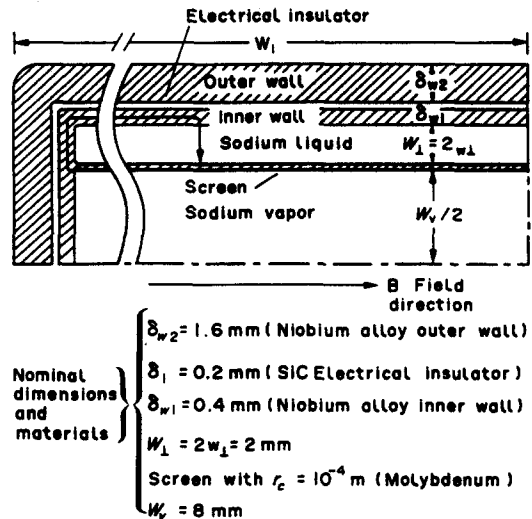


Fig. 38. Cross-sectional view of the sodium heat pipe.

where w_h is the half width of the flow channel in a direction parallel to the magnetic field B , and δ is the channel wall thickness. The minimization of $(dP/dz)_B$ therefore requires the minimization of the wall conduction ratio C , implying that the heat pipe should be of a flattened design rather than round, and with the long face parallel to the magnetic field. Further considerations of the heat pipe design require the addition of an electrically insulating wall between the outer and inner walls of the pipe to reduce the circulation of eddy currents into the liquid metal pool, nonuniform heat generation within the blanket, access of heat pipes into the pool, material compatibility and structural considerations (the helium coolant pressure on the condenser surface is 30 atm, the lithium pool pressure on the evaporator surface is 2–5 atm, whereas the sodium operating pressure in the heat pipe is about 0.2 atm at 1000 K). Figure 37 illustrates the final heat pipe design with the cross-sectional view shown in Fig. 38. The safe normal power of each heat pipe is 47 kW (Fig. 39) at 1000 K, which with a safety factor of 1.5, would require 120,000 heat pipes for a fusion reactor of 3,500 MW. Each heat pipe can also support a power of 70 kW at 1040 K by operating close to the dryout power level (see Fig. 39). The heat pipe design, however, did not include the flooding limit calculation as this is unknown in flat channel wick heat pipes.

The use of copper/water heat pipes for maintaining an accurate temperature control of pin holes and X-ray beam position monitors at the National Synchrotron Light Source at the Brookhaven National Laboratory is described in [54] and [55]. In these applications the cooling with heat pipes is preferable to other means because of their capability to remove high localized thermal fluxes and vibrations of the X-ray detector and position monitoring systems.

3.4. Thermal control of electronic equipment

The current trend in electronics is components miniaturization through very large scale integration and microminiaturization into the three-dimensional solid state lattices [56, 57]. This development trend will not only require an accurate temperature control of devices to maintain high components reliability, but also the removal of thermal fluxes in excess of 50 W cm^{-2} . Peterson [58] discussed some heat pipes for the thermal control of electronic equipment and summarized three methods of the heat pipe use: (1) use of large heat pipes for the heat removal from enclosures; (2) use of heat pipes with directly mountable electronic components; (3) use of micro heat pipes (heat pipes in which the capillary channel is only slightly larger than the molecular diameter of the working fluid) embedded in the material substrate within the three-dimensional chip. With the current technology in micromachining [59], the use of micro heat pipes will no doubt develop soon into a technology. Figure 40 illustrates the utilization of VCHP in the cooling of circuit modules of a computer [60]. In the arrangement shown, the circuit module (12) is connected by the

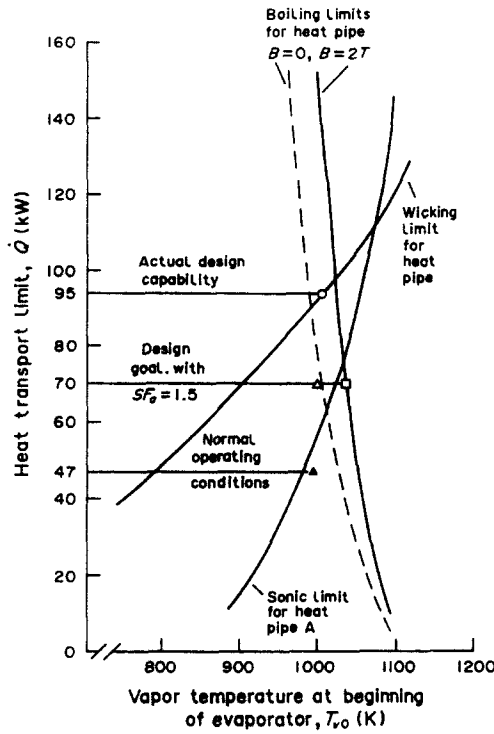


Fig. 39. Sodium heat pipe operating limits.

horizontal heat pipe system (18) to the vertical heat exchange unit (22) which by itself may be a heat pipe device. The thermal management of high power printed wiring boards by means of heat pipes for the use in avionic systems is discussed in [61] and [62] for two different designs: heat pipes embedded into the circuit card substrates and heat pipes manufactured into the substrates (the vapor chamber substrate). The water and methanol tests show that the integration of heat pipes into substrates gives a superior thermal performance to that of the embedded heat pipe design configurations. The future decreases in the manufacturing costs should, therefore, make such a technology much more desirable. In another application shown in Fig. 41 [63], the circuit chip (14) is connected to a bellows type heat pipe (22). The grooved condenser bottom surface (18) is made of silicon and soldered to the chip to provide an effective heat transfer through the capillary liquid pumping from the wick screen (24) of the heat pipe. The bellows heat pipe is effective in reducing the transmission of stresses from the cooling system (26) of the pipe (condenser) to the chip. The

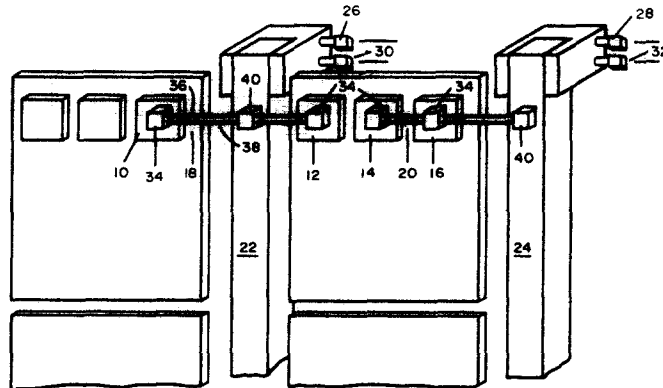


Fig. 40. Heat pipe links for cooling of computer modules.

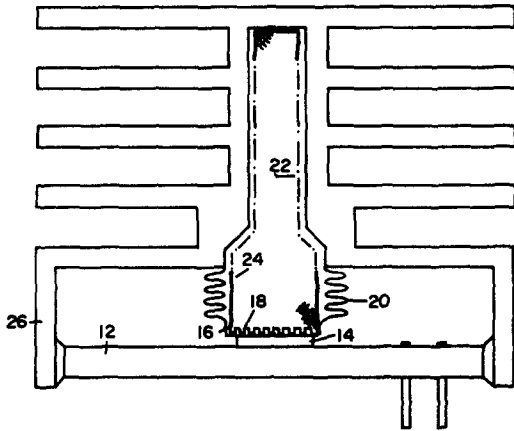


Fig. 41. Bellows heat pipe in cooling of silicon structures.

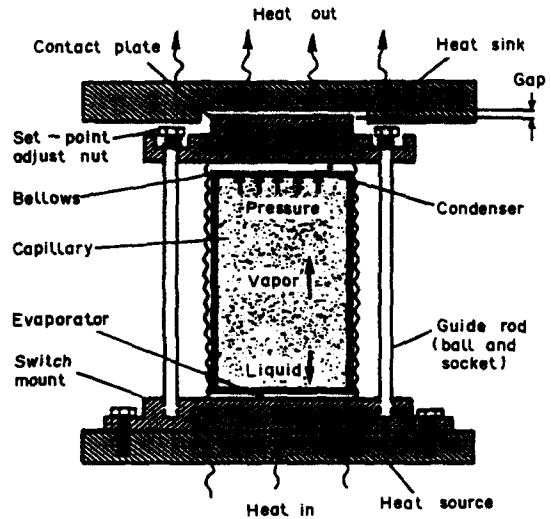


Fig. 42. Heat pipe thermal switch.
Copyright ©AIAA; reprinted with permission.

use of heat pipes, instead of fins, to cool the thermal control modules of a recent IBM computer is discussed in [64], whereas Peterson [65] considered the modeling of a bellows type heat pipe acting as a thermal switch. The thermal switch is illustrated in Fig. 42. Its sizing must account for the bellows expansion owing to the internal heat pipe pressure, thermal expansion of the bellows vessel and the stretching effect within the bellows material. The overall design of a thermal switch should involve, therefore, the use of a total elongation relation as explained above and the usual formulas expressing the heat pipe limited operations.

4. HEAT PIPES IN SPACE APPLICATIONS

Each subsystem of a space system should be reliably designed because of the high cost of building, launching and maintaining such a system in space. Moreover, a space system should also be resistant to the micrometeoroid damage. For these reasons, heat pipes have considerable utility for variety of spacecraft applications, ranging from the thermal control of spacecrafts to the transfer of heat from space power sources to heat sinks. The United States is currently designing a space station and considering various options for large space power systems and future manned and unmanned missions [66–69]. Figure 43 shows the configuration of the current version of the space station [68].

4.1. Thermal control

The thermal control of the space station will require the control of various modules and maintaining reliable operation of the equipment on board. The space station's power requirement may start at about 75 kW and expand to about 300 kW, which will require the dissipation of large quantities of heat into space through the thermal radiators (see Fig. 43). These thermal radiators are envisaged to be constructed from modular heat pipe units and assembled in space into the Space Constructable Radiators (SCR) [70, 71]. Some of the heat pipes considered for this design include monogroove, tapered artery, axially grooved and dual slot as discussed in Section 2. For the thermal control of the space station's modules, the ammonia heat pipes appear to be preferable at present due to their high performance level from -50 to 150°C and compatibility with the lightweight aluminum material. The monogroove, ATAG and tapered artery heat pipes can all be manufactured economically by an extrusion process. The design of the SCR and cold plates using the monogroove heat pipes is discussed in [72, 73], while the application of axially grooved pipes in various other spacecrafts is discussed in [74]. As an alternative to the design of SCR by the finned surfaces attached to high performance heat pipes, Hughes Aircraft [75, 76] has been developing a

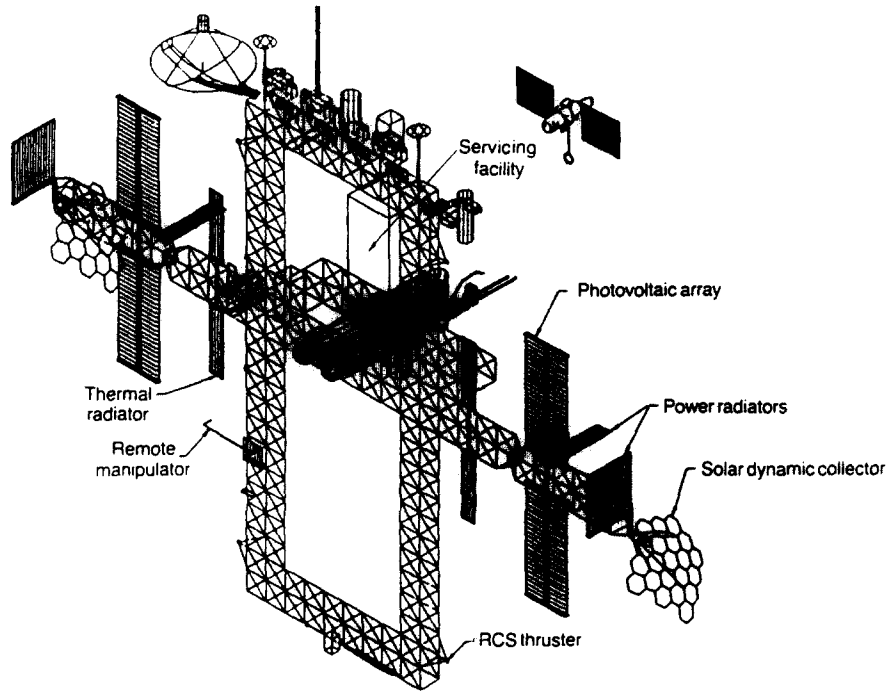


Fig. 43. Space station configuration.
Copyright ©AIAA; reprinted with permission.

honeycomb heat pipe panel (Fig. 44) which may be integrated either with the high performance heat pipes or form an integral heat pipe assembly (Fig. 45).

For the purpose of providing thermal management of multikilowatt capacity spacecrafts, the OAO Corporation has been developing a Capillary Pump Loop (CPL) heat pipe system [77-80] as schematically illustrated in Fig. 46. This system consists of evaporators which are constructed of unidirectional flow heat pipes with porous wick structure, and condensers without the wick material. The fluid pumping through the system is accomplished by the capillary pumping action in the wick and by connecting heat pipe evaporators and condensers in parallel, within a single loop, to minimize pressure drops and accommodate multiple heat sources and sinks. Each heat pipe

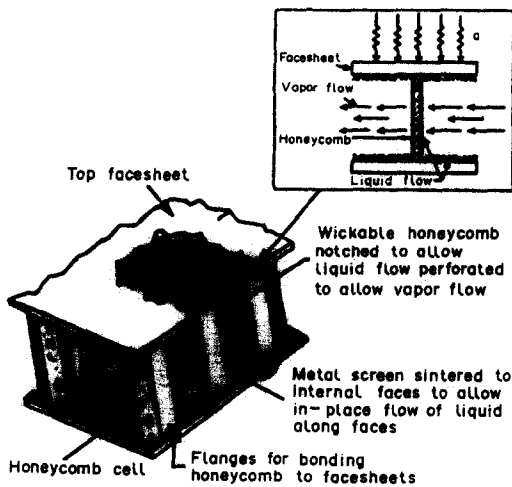


Fig. 44. Honeycomb heat pipe panel configuration.
Copyright ©AIAA; reprinted with permission.

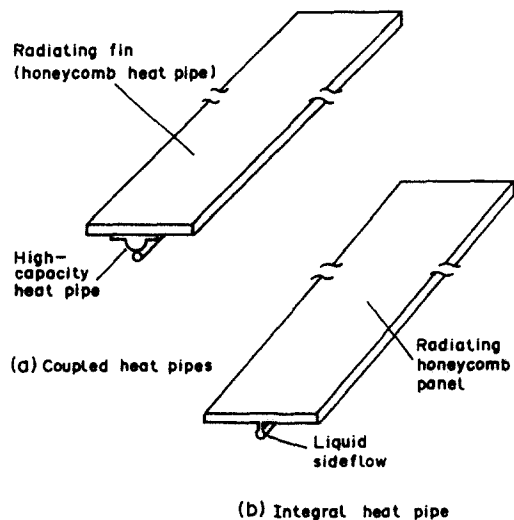


Fig. 45. Integration options for the honeycomb panels.
Copyright ©AIAA; reprinted with permission.

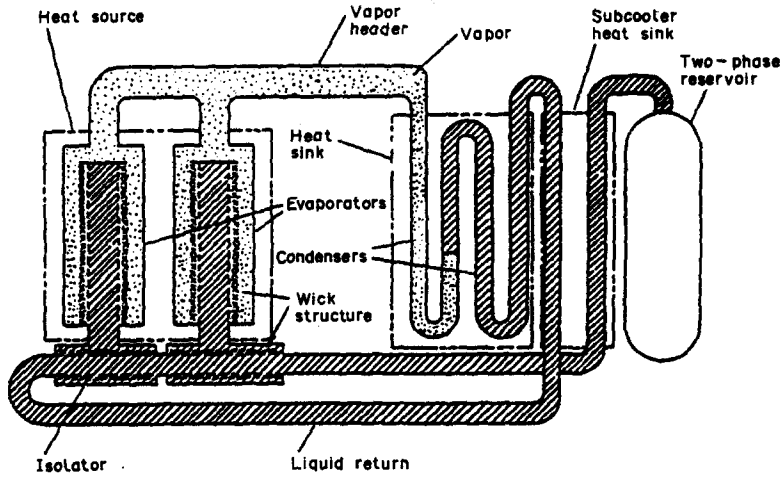


Fig. 46. Capillary pumped loop system concept.
Copyright ©AIAA; reprinted with permission.

evaporator consists of an axially grooved tubing outer shell which is packed with a wick material so that the liquid flows radially to the fin tips. The fin tips provide the surface area for evaporation, whereas the grooves in the tube shell provide for the vapor flow as shown in Fig. 47. To allow for the fluid inventory and temperature control and to prevent wick depriming, the CPL system is also equipped with a reservoir and vapor isolators (see Figs 46 and 47). Using ammonia as the working fluid, the CPL system operation was demonstrated in $1g$ [77, 78] and $0g$ [79] environments. The system testing involved eight parallel evaporators and six parallel condensers in a single loop and demonstrated the heat transport capacity of up to 70 kW-m , with each individual heat pipe managing 1.7 kW with a radial heat flux of 15 W cm^{-2} , for a wide range of operational requirements. The application of the CPL heat pipe systems to the space station, satellites and high powered spacecrafts is discussed in [80].

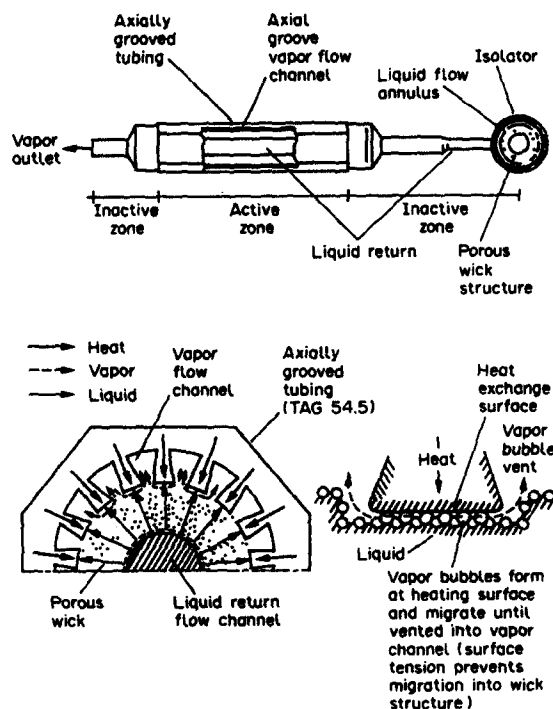


Fig. 47. Heat pipe evaporator configuration in the capillary pumped loop system.

4.2. Space radiators for the solar dynamic and nuclear power systems

It is currently envisaged that the space station's electrical power requirement from approximately 75 to 300 kW will be supplied through a hybrid system involving a photovoltaic system and a pair of solar dynamic power modules, using either an organic Rankine cycle or a closed Breyton cycle as shown in Fig. 43. A solar dynamic system sized for a net generating capacity of 25 kW_e and an efficiency of conversion of 20%, will require the rejection of 125 kW of thermal energy through the radiators. As the required radiator area decreases with an increasing radiator temperature, the heat pipes envisaged for use in these radiators will be operating at higher temperatures than those of the thermal radiators discussed above [69]. Above 100°C the methanol and water give a superior thermal performance to that of ammonia, with the methanol performance deteriorating above about 150°C. The water, however, has a freezing temperature problem which makes it undesirable for use in space, whereas the methanol is not compatible with aluminum. For these reasons, the radiators of solar dynamic systems are envisaged to be constructed from the stainless steel heat pipes with the working fluid methanol operating from 100 to 150°C and integrated into the SCR as illustrated, for example, in Fig. 13.

Vanlandingham [66] envisages the initial large capacity (about 300 kW_e) space power system to be of the nuclear type, for ease of testing on Earth and transporting into the space by the space shuttle. The latter requirements dictate a very compact system design with the nuclear core generating heat at about 1000 K [81–83]. Due to this, Merrigan *et al.* [10] discuss the typical requirements of a space nuclear reactor as: (1) 100–200 W cm⁻² radial power density; (2) 10 kW cm⁻² axial power density; (3) long adiabatic sections to provide separation between the nuclear core and conversion system; (4) an operation close to the material limits. As a consequence, they note that high temperature heat pipes for cooling of space nuclear reactors offer several favorable characteristics such as self-regulation and start-up, decay heat removal after the reactor shut down and a high reliability. The lithium heat pipe discussed in Section 2 [10, 11] was designed with the above performance requirements in mind.

Merrigan *et al.* [81] discuss a self-deployed membrane heat pipe radiator concept, shown in Fig. 48, using sodium at 1000 K. To test the feasibility, they constructed a heat pipe from stainless steel with three layers of 100 mesh screen, $L_e = 0.15$ m, flexible length of 0.45 m, and $L_c = 0.2$ m. During the testing at a room temperature (frozen state) and at 1000 K, they flexed the heat pipe repeatedly through an angle of 180° in horizontal and vertical (evaporator up) positions without experiencing any performance degradation for axial test powers up to 2 kW cm⁻².

Avery [82] considers the use of austenitic stainless steels and zirconium alloys for heat pipes using potassium (770–870 K) as the working fluid in graphite reactors. The heat pipe material selection requires the consideration of the nuclear cross section, compatibility with the working fluid and external environment, operating temperature, creep strength, resistance to radiation damage and fabricability. Zirconium has a low thermal neutron cross section and is generally used up to 670 K, while austenitic stainless steels are compatible with potassium up to 920 K. The compatibility test results on the potassium graphite reactions showed no significant effect, whereas the 793 K carbon reacted with the zirconium alloy and it would yield a 1% degradation of the heat pipe wall thickness after 20 years.

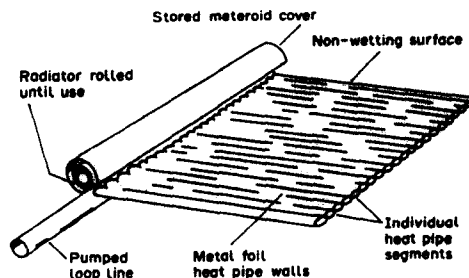


Fig. 48. Self-deployed membrane sodium heat pipe radiator concept, Merrigan *et al.* (1984).

Table 10. Axially grooved heat pipe technology
Copyright ©AIAA; reprinted with permission

Type	Size (in) & material	Heat Transport* (W in)	Static wicking* (in)	External shapes
GSFC/ATS	0.625 Al	5,500	0.50	Round, flat
OAO/ATS-I	0.560 Al	10,500	0.55	Round, flat
OAO/ATS-II	0.520 Al	9,400	0.49	Round, flat
TAG 1-15	0.250 Al	1,270	1.45	Round
TAG 2-5	0.313 Al	2,100	0.54	Round
TAG 5-3	0.375 Al	3,100	0.31	Round, flat
TAG 6-16	0.500 Al	5,900	1.63	Round
TAG 10-11	0.563 Al	10,200	1.09	Round
TAG 12-8	0.625 Al	11,900	0.84	Round, flat
TAG 54-5	1.125 Al	53,700	0.48	Round, flat
SIG-Cu	0.313 Cu	2,450	1.10	Round
HEPP-SST	0.438 ss	2,550	0.53	Round

*All values are for ammonia at 0°C except for the type SIG-Cu whose values are for 90°C water.

An analysis of sodium and potassium heat pipes for space radiators operating from 700–1600 K is performed in [83]. The heat pipe geometry used for the study involved an annular configuration with a thin co-axial wick structure (400–500 mesh screen), a 0.5 mm annular gap for $D_i = 12.7$ mm tube and scaled for larger tube diameters, and different lengths of the evaporator section (determined by the allowable radial power limit) and the condenser section (determined by the heat pipe performance limits). The analysis was verified with the tests of lithium [81] and the results show that a potassium heat pipe radiator element of length up to 30 m and $L/D = 300$ is possible, whereas that for sodium may have useful lengths up to 40 m and $L/D = 800$. For the latter heat pipe design, the calculated power throughput is 125kW.

4.3. Satellites

The specific heat pipes used in satellites depends on whether the satellite is a spinner or 3 axis controlled (non-rotating). Typical satellite powers may range from 50 W to 10 kW (the 1990's design). Brennan and Melak [74] discuss the use of axially grooved heat pipe technology (Table 10) in the Ultraviolet Imaging Telescope, Spartan 2 White Light Coronagraph, Faint Object Spectrograph (instrument on a space telescope), and Direct Broadcast and Ku-Band Communication Satellites. The flexible heat pipes [9] have a particularly useful application in satellites for the thermal management of heat and temperature. Of particular importance in space satellites are cryogenic heat pipes to maintain low detector temperatures (for the reduction of thermal noise in electronic detectors). Peterson and Compagna [84] discuss the use of various cryogenic fluids for heat pipes, while the use of VCHP in satellites may be found in [85].

5. CONCLUSIONS

The recent heat pipe research and development activities in the Americas are mainly associated with the development of high heat transfer performance heat pipes for space applications. The heat pipes being developed vary from cryogenic applications (cooling of infrared detectors) to the cooling of future nuclear reactor cores of the space power systems by using lithium as the working fluid at very high temperatures. Heat pipe developers mainly use simple design models for the heat pipe performance optimization before building and testing the prototypes. The need to understand the transient heat pipe behavior under rapid start ups and shut downs has provided some impetus for the transient testing and modeling. The transient modeling of heat pipes, however, is not in step with the technological requirements. Very high performance heat pipes will have to operate with large radial and axial heat fluxes, which will require the development of good heat pipe simulation models to determine the optimum heat pipe geometry for a given application before actually building and testing them.

Acknowledgements—In preparing the information for the paper the author would like to acknowledge the help of the following individuals: A. Basiulis, R. P. Bobco, P. Brennan, J. Jones, J. Ku, B. S. Larkin, P. J. Marto, G. P. Peterson, R. Ponnappan, C. L. Tien, and A. J. S. Timins.

REFERENCES

1. J. Alario, R. Haslett and R. Cosson, The monogroove high performance heat pipe, *Prog. Astron. Aeronautics* **83**, 305–324 (1982).
2. H. R. Holmes and A. R. Feild, The gas-tolerant high-capacity tapered artery heat pipe, *AIAA/ASME 4th Joint Thermophysics and Heat Transfer Conference*, Paper AIAA-86-1343. Boston, Massachusetts (1986).
3. R. F. G. Richter, P. J. Brennan and J. G. Rankin, Development of an advanced trapezoidal axially grooved (ATAG) heat pipe, *AIAA/ASME 4th Joint Thermophysics and Heat Transfer Conference*, Paper AIAA-86-1342. Boston, Massachusetts (1986).
4. J. Alario, R. Haslett and R. Kosson, Dual channel axial heat pipe, U.S. Patent No. 4470451 (1984).
5. A. W. Carlson and E. Gustafson, Heat pipe radiator technology for space power systems, *AIAA/ASME 4th Joint Thermophysics and Heat Transfer Conference*, Paper AIAA-86-1300. Boston, Massachusetts (1986).
6. R. Ponnappan and E. T. Mahefkey, Development of a double-wall artery high-capacity heat pipe, *Prog. Astron. Aeronautics* **86**, 202–221 (1983).
7. R. Ponnappan, J. E. Beam and E. T. Mahefkey, Improved double-wall artery high capacity heat pipe, *J. Spacecraft Rockets* **22**, 592–597 (1985).
8. R. Ponnappan, J. E. Beam and E. T. Mahefkey, Priming and flow visualization in the double wall artery heat pipe, *Proc. 8th International Heat Transfer Conference* **6**, 3079–3084. Hemisphere (1986).
9. R. M. Shaubach and N. J. Gernert, High performance flexible heat pipes, *AIAA 20th Thermophysics Conference*, Paper AIAA-85-1085. Williamsburg, Virginia (1985).
10. M. A. Merrigan, E. H. Martinez, E. S. Keddy, J. E. Runyan and J. E. Kemme, Performance demonstration of a high power space reactor heat pipe design, *Intersociety Energy Conversion Engineering Conference* **4**, 1874–1879 (1983).
11. M. A. Merrigan, J. E. Runyan, H. E. Martinez and E. S. Keddy, Development and test of a space reactor core heat pipe, *AIAA Thermophysics Conference*, Paper AIAA-83-1530. Montreal, Canada (1983).
12. K. A. R. Ismail, C. Y. Liu and N. Murcia, Heat pipe with modified internal geometry, *Alternative Energy Sources V*, Part A, pp. 455–461. Elsevier (1983).
13. K. A. R. Ismail, C. Y. Liu and R. G. B. Silva, Heat pipes with porous sintered wicks, *Alternative Energy Sources VI*, pp. 359–364. Hemisphere (1985).
14. G. P. Peterson and L. S. Fletcher, Effective thermal conductivity of sintered heat pipes wicks, *AIAA/ASME 4th Joint Thermophysics and Heat Transfer Conference*, Paper AIAA-86-1362. Boston, Massachusetts (1986).
15. M. A. Merrigan and E. S. Keddy, High temperature heat pipes for waste heat recovery, *J. Energy* **6**, 298–303 (1982).
16. B. S. Larkin, Enhancement of boiling at low temperatures in wickless copper/water heat pipes, *Proc. 6th International Heat Pipe Conference*, pp. 500–504. Grenoble, France (1987).
17. G. T. Colwell and W. S. Chang, Measurements of the transient behavior of a capillary structure under heavy thermal loading, *Int. J. Heat Mass Transfer* **27**, 541–551 (1984).
18. W. S. Chang and G. T. Colwell, Mathematical modeling of the transient operating characteristics of a low temperature heat pipe, *Numerical Heat Transfer* **8**, 169–186 (1985).
19. J. E. Beam, Transient heat pipe analysis, *AIAA 20th Thermophysics Conference*, Paper AIAA-85-0936. Williamsburg, Virginia (1985).
20. J. H. Ambrose, L. C. Chow and J. E. Beam, Transient heat pipe response and rewetting behavior, *AIAA/ASME 4th Joint Thermophysics and Heat Transfer Conference*, Paper AIAA-86-1359. Boston, Massachusetts (1986).
21. B. Cullimore, Modeling of transient heat pipe effects using a generalized thermal analysis program, *AIAA 20th Thermophysics Conference*, Paper AIAA-85-0938 (1985).
22. D. E. Tilton, L. C. Chow and E. T. Mahefkey, Transient response of a liquid metal heat pipe subjected to external loading at the condenser, *AIAA/ASME 4th Joint Thermophysics and Heat Transfer Conference*, Paper AIAA-86-1271. Boston, Massachusetts (1986).
23. D. L. Jacobson and B. S. Lou, Sodium, Inconel 600 heat pipe life test analysis, *AIAA/ASME 4th Joint Thermophysics and Heat Transfer Conference*, Paper AIAA-86-1272. Boston, Massachusetts (1986).
24. R. P. Bobco, Variable conductance heat pipes: A first order model, *J. Thermophys.* **1**, 35–42 (1987).
25. R. P. Bobco, An extended model for VCHP analysis: Zero-to-full heat loads, Paper submitted to *AIAA 22nd Thermophysics Conference*, Honolulu, Hawaii (1987).
26. D. K. Edwards and B. D. Marcus, Heat and mass transfer in the vicinity of the vapor–gas front in a gas loaded heat pipe, *J. Heat Transfer* **94C**, 155–162 (1972).
27. M. D. Kelleher, Analysis of the effects of gravity on the operation of a vertical gas loaded heat pipe, Personal communication with P. J. Marto, Naval Postgraduate School (1987).
28. T. Fukano, S. J. Chen and C. L. Tien, Operating limits of the closed two-phase thermosyphon, *Proc. ASME/ASME Thermal Engineering Conference* **1**, 95–101 (1983).
29. T. Fukano, K. Kadoguchi and C. L. Tien, Oscillation phenomena and operating limits of the closed two-phase thermosyphon, *Proc. 8th International Heat Transfer Conference*, **5**, 2325–2330. Hemisphere (1986).
30. F. Dobran, Steady state characteristics and stability thresholds of a closed two-phase thermosyphon, *Int. J. Heat Mass Transfer* **28**, 949–957 (1985).
31. J. I. Ramos and F. Dobran, Stability analysis of a closed thermosyphon model, *Appl. Math. Modelling* **10**, 61–67 (1986).
32. J. G. Reed and C. L. Tien, Modeling of the two-phase closed thermosyphon, *J. Heat Transfer*, **109**, 722–730 (1987).
33. S. J. Chen, J. G. Reed and C. L. Tien, Reflux condensation in a two-phase closed thermosyphon, *Int. J. Heat Mass Transfer* **27**, 1587–1594 (1984).
34. K. Hijikata, S. J. Chen and C. L. Tien, Non condensable gas effect on condensation in a two-phase closed thermosyphon, *Int. J. Heat Mass Transfer* **27**, 1319–1325 (1984).
35. P. F. Peterson and C. L. Tien, A miniature wet bulb technique for measuring gas concentrations in condensing or evaporating systems, *Experimental Heat Transfer* **1**, 3843 (1987).
36. V. A. Cundy and L. N. Ha, The characterization of a gravity assisted heat pipe with internal two-phase parallel flow throughout, *Thermal Sci.* **16**, 599–612. Hemisphere (1983).
37. M. Katsuta, A. S. Wanniarachchi and P. J. Marto, Condensation heat transfer measurement in co-axial rotating heat pipe, Personal communication with P. J. Marto, Naval Postgraduate School (1987).

38. C. C. Silverstein, Correlation of heat pipe heat transport limits with vapor pressure, *AIAA 20th Thermophysics Conference Paper AIAA-85-0939*. Williamsburg, Virginia (1986).
39. F. Haug and C. A. Busse, Pressure recovery in a cylindrical heat pipe at high radial Reynolds numbers and at high Mach numbers, *AIAA 20th Thermophysics Conference, Paper AIAA-85-0980*. Williamsburg, Virginia (1985).
40. C. A. Busse and F. C. Prenger, Numerical analysis of the vapor flow in cylindrical heat pipes, *Proc. 5th International Heat Pipe Conference 1*, 214–219 (1984).
41. F. C. Prenger, E. S. Keddy and J. T. Sena, Performance characteristics of gravity assisted potassium heat pipes, *AIAA 20th Thermophysics Conference, Paper AIAA-85-1086*. Williamsburg, Virginia (1985).
42. R. L. Kosson and W. Harwell, The Marangoni effect in axially grooved variable conductance heat pipes, *Prog. Astron. Aeronautics 86*, 222–238 (1983).
43. D. A. Littwin and D. B. Willis, The use of heat pipes to conserve energy in petroleum refineries, *Energy Progress 5*, 198–202 (1985).
44. G. P. Peterson, Heat pipe exchangers in waste heat recovery, *Industrial Pollution Control Conference*, ASME, 95–98 (1983).
45. C. H. Johnson and E. Zeigler, Design and evaluation of a heat pipe heat exchanger, *Energy Technology IX*, pp. 389–396. Government Institute Inc. (1982).
46. F. E. Becker, E. F. Searight and A. I. Zakak, High efficiency space heating systems utilizing heat pipe heat exchangers, *International Gas Research Conference*, pp. 695–702 (1983).
47. R. James, Heat pipe system runs hot and cold energy savings, *Energy Management Technology*, pp. 26–27 (1986).
48. J. P. Hodge, Industrial innovative ways to save energy in new buildings, *Heating/Piping/Air Conditioning*, May, pp. 71–82 (1986).
49. M. Scofield and J. R. Taylor, A heat pipe economy cycle, *ASHRAE J.* October, pp. 35–40 (1986).
50. Y. K. Chuah and F. Kreith, A heat pipe Rankine engine, *Intersociety Energy Conversion Engineering Conference 3*, 616–619 (1985).
51. A. R. Foster, G. J. Kowalski and G. W. Lopez, Solar heat pipe water heater, *Alternative Energy Sources VI*, pp. 337–351. Hemisphere, New York (1985).
52. K. A. R. Ismail and C. Y. Liu, Steam generation via solar heat pipes, *Alternative Energy Sources VI* pp. 353–357. Hemisphere, New York (1985).
53. N. L. Schwartz and M. A. Hoffman, A heat pipe concept for cooling a liquid-pool blanket of a tandem mirror fusion reactor, *Nuclear Technology/Fusion 4*, 479–490 (1983).
54. D. Shu, P. Mortazavi, H. Rarback and M. R. Howells, Application of heat pipes for high thermal load beam lines, BNL 36974. Brookhaven National Laboratory, Upton, New York (1985).
55. P. Mortazavi, M. Woodle, H. Rarback, D. Shu and M. Howells, High flux photon beam monitor, BNL 36903. Brookhaven National Laboratory, Upton, New York (1985).
56. A. J. Blodgett Jr, Microelectronic packaging, *Scientific Am.* July, 86–96 (1983).
57. G. H. Dohler, Solid state superlattices, *Scientific Am.* November, pp. 144–151 (1983).
58. G. P. Peterson, Heat pipe thermal control of electronic components, *AIAA 20th Thermophysics Conference, Paper AIAA-85-0937*. Williamsburg, Virginia (1985).
59. J. B. Angell, C. Terry and P. W. Barth, Silicon micromechanical devices, *Scientific Am.* April, 44–55 (1983).
60. N. G. Aakalu and R. A. Carlen, Heat pipe links for water-cooled computer circuit assemblies, *IBM Technical Disclosure Bulletin 27*, 3551–3552 (1984).
61. A. Basiulis, H. Tanzer and S. McCabe, Thermal management of high power PWB's through the use of heat pipe substrates, *6th Annual International Packaging Conference*. San Diego, California (1986).
62. G. W. Scott and H. J. Tanzer, Evaluation of heat pipes for conduction cooled level II avionic packages, *Heat Transfer in Electronic Equipment*, ASME, 67–75. New York (1986).
63. J. M. Eldridge and K. E. Peterson, Heat pipe vapor cooling etched silicon structure, *IBM Technical Disclosure Bulletin 25*, 4118–4119 (1983).
64. Author Unknown, Heat pipe pin fin cap, *IBM Technical Disclosure Bulletin 27*, 6726 (1985).
65. G. P. Peterson, Analytical development and computer modeling of a bellows type heat pipe for the cooling of electronic components, *ASME Winter Annual Meeting, Paper 86-WA/HT-69*, Anaheim, California (1986).
66. E. E. Vanlandingham, The NASA space power technology program, *Intersociety Energy Conversion Engineering Conference 3*, 1405–1410 (1988).
67. R. R. Barthelemy, L. D. Massie and W. U. Borger, Military space power systems technology for the twenty-first century, *Intersociety Energy Conversion Engineering Conference 3*, 1401–1404 (1986).
68. C. Desanctis, C. Priest and W. Wood, Space station overview, *AIAA 25th Aerospace Sciences Meeting, Paper AIAA-86-0315*. Reno, Nevada (1987).
69. J. A. Sadunas and A. Lehtinen, Thermal management systems options for high power space platforms, *AIAA 20th Thermophysics Conference, Paper AIAA-85-1047*. Williamsburg, Virginia (1985).
70. J. A. Oren and R. L. Cox, Thermal management for large space platforms, *J. Spacecraft Rockets 19*, 278–283 (1982).
71. T. Baer, Space station thermal control, *Mech. Engng* December, pp. 22–33 (1984).
72. P. J. Otterstedt, J. Hussey and J. P. Alario, Space constructable on-orbit assembly, *AIAA 20th Thermophysics Conference, Paper AIAA-85-1048*. Williamsburg, Virginia (1985).
73. F. Edelstein, R. Brown and K. Koubek, Design and test of a two-phase monogroove cold plate, *AIAA 20th Thermophysics Conference, Paper AIAA-85-0978*. Williamsburg, Virginia (1985).
74. P. Brennan and A. Melak, Thermal design of current spacecraft and Shuttle payloads utilizing heat pipe technology, *AIAA 20th Thermophysics Conference, Paper AIAA-85-1008*. Williamsburg, Virginia (1985).
75. H. J. Tanzer and G. L. Fleischman, Honeycomb panel heat pipe development for space radiators, *AIAA 20th Thermophysics Conference, Paper AIAA-85-0978*. Williamsburg, Virginia (1985).
76. H. J. Tanzer, R. Cerza Jr and J. B. Hall, High capacity demonstration of honeycomb panel heat pipes, *16th Intersociety Conference on Environmental Systems*. San Diego, California (1986).
77. E. J. Krolczek and J. Ku, Design, development and test of a capillary pump loop heat pipe, *AIAA 19th Thermophysics Conference, Paper AIAA-84-1720*. Snowmass, Colorado (1984).

78. J. Ku, E. J. Kroliczek and W. J. Taylor, Functional and performance tests of two capillary pumped loop engineering models, *AIAA/ASME 4th Joint Thermophysics and Heat Transfer Conference*, Paper AIAA-86-1248. Boston, Massachusetts (1986).
79. J. Ku, E. J. Kroliczek, D. Butler, R. B. Schweickart and R. McIntosh, Capillary pumped loop GAS and hitchhiker flight experiments, *AIAA/ASME 4th Joint Thermophysics and Heat Transfer Conference*, Paper AIAA-86-1249. Boston, Massachusetts (1986).
80. D. R. Chalmers, J. J. Pustay and C. B. Moy, Application of capillary pumped loop heat transport systems to large spacecraft, *AIAA/ASME 4th Joint Thermophysics and Heat Transfer Conference*, Paper AIAA-86-1295. Boston, Massachusetts (1986).
81. M. A. Merrigan, E. S. Keddy, J. T. Sena and M. G. Elder, Heat pipe technology development for high temperature space radiator applications, *Intersociety Energy Conversion Engineering Conference 1*, 592-597 (1984).
82. J. G. Avery, Heat pipe material compatibility concerns for a remote reactor, *Intersociety Energy Conversion Engineering Conference 1*, 1459-1465 (1985).
83. M. A. Merrigan, Heat pipe design for space power heat rejection applications, *Intersociety Energy Conversion Engineering Conference 3*, 1993-1998 (1986).
84. G. P. Peterson and G. L. Compagna, Cryogenic heat pipes in spacecraft applications, *AIAA/ASME 4th Joint Thermophysics and Heat Transfer Conference*, Paper AIAA-86-1254. Boston, Massachusetts (1986).
85. Lightweight variable conductance heat pipes for space applications, March 1986, Hughes Aircraft Company Report.